


# FUEL ROD MATERIAL BEHAVIOR DURING TEST PCM-1

BEVERLY A. COOK

June 1979

790814a28

 **EG&G** Idaho, Inc.



IDAHO NATIONAL ENGINEERING LABORATORY

**DEPARTMENT OF ENERGY**

IDAHO OPERATIONS OFFICE UNDER CONTRACT DE-AC07-76IDO1570

631 154

NOTICE

This report was prepared as an account of work sponsored by an agency of the United States Government. Neither the United States Government nor any agency thereof, or any of their employees, makes any warranty, expressed or implied, or assumes any legal liability or responsibility for any third party's use, or the results of such use, of any information, apparatus, product or process disclosed in this report, or represents that its use by such third party would not infringe privately owned rights.

The views expressed in this report are not necessarily those of the U.S. Nuclear Regulatory Commission.

Available from  
National Technical Information Service  
Springfield, Virginia 22161  
Price: Printed Copy A06; Microfiche \$3.00

The price of this document for requesters outside the North American continent can be obtained from the National Technical Information Service.

631 155

# FUEL ROD MATERIAL BEHAVIOR DURING TEST PCM-1

Beverly A. Cook

EG&G Idaho, Inc.  
Idaho Falls, Idaho 83401

Published June 1979

PREPARED FOR THE  
U.S. NUCLEAR REGULATORY COMMISSION  
AND THE U.S. DEPARTMENT OF ENERGY  
IDAHO OPERATIONS OFFICE  
UNDER CONTRACT NO. DE-AC07-76IDO1570  
NRC FIN NO. A6041

## ACKNOWLEDGMENTS

The author thanks Ms. P. B. Reed for assistance in preparing the figures, and Drs. R. R. Hobbins and S. L. Seiffert for their extensive review.

## ABSTRACT

This report presents the analysis of the fuel rod materials behavior based on the postirradiation examination of the Test PCM-1 fuel rod from the Power-Cooling-Mismatch (PCM) Test Series. The test objective was to evaluate the behavior of a single pressurized water reactor (PWR) type fuel rod subjected to film boiling operation at high power following rod failure. The failure mechanisms and subsequent breakup of the fuel and cladding are discussed. The fuel rod cladding temperature profile is determined by metallographic examination of cladding microstructures and calculations based on kinetic correlations of the cladding external surface reaction layers with the duration of film boiling. Cladding-coolant and cladding-fuel interactions are investigated by metallographic and microprobe examination and chemical analysis of the cladding. Fuel restructuring and chemical changes are also addressed.

## SUMMARY

The materials behavior of the Test PCM-1 fuel rod was analyzed on the basis of the postirradiation examination. The test was part of the Power-Cooling-Mismatch Test Series conducted by the Thermal Fuels Behavior Program of EG&G Idaho, Inc., and sponsored by the United States Nuclear Regulatory Commission's Fuel Behavior Research Program. The test was designed to evaluate the behavior of a single PWR-type fuel rod subjected to film boiling operation at high power following rod failure.

Following operation at low power levels for preconditioning and power calibration purposes, the fuel rod peak power was increased to 69 kW/m to initiate film boiling and held until 280 seconds from the start of the ramp. The power was then raised to 78 kW/m and held for an additional 640 seconds. Instrumentation indicated initial rod failure at 520 seconds and severe rod breakup at shutdown. Posttest examination revealed cladding failure due to embrittlement and significant cladding breakup during film boiling operation. Fuel fragmentation occurred primarily during quenching at test shutdown, resulting in the loss of 24% of the fuel stack into the coolant. Some structural integrity was maintained in unclad fuel sections.

The fuel rod temperature profile was determined. Cladding melting occurred over as much as 31% of the fuel rod. The molten fuel region extended from at least 0.30 m (with a melt radius of 77%) to 0.67 m (melt radius 36%). A 180- to 220-K circumferential temperature gradient was noted at two of the elevations examined, probably due to the cooling effect of the thermocouples attached to the fuel rod.

Extensive fuel-cladding and cladding-coolant reactions occurred. Large duplex U-Zr reaction layers formed between the fuel and cladding. The cladding then oxidized the  $ZrO_2$ , leaving a uranium gradient through a portion of the cladding. Molten fuel interacted with the cladding at some locations, resulting in zirconium as far as 1.6 mm into the fuel pellet and uranium halfway through the cladding wall. Some sections of the cladding that were completely oxidized to  $ZrO_2$  remained intact.

The continual oxidation of the cladding insulated the fuel pellets and subsequently raised the fuel temperatures. Molten fuel radii as large as 85% were found. The increasing fuel temperatures may have been the cause of the unusual porosity distribution observed. Oxidation of the  $UO_2$  fuel occurred. The fuel was  $UO_2 + x$  at operating temperature, and  $U_4O_9$  at ambient temperature posttest. The addition of oxygen to the  $UO_2$  fuel accelerated grain growth and decreased the fuel melting temperature.

# CONTENTS

ACKNOWLEDGMENTS .....	ii
ABSTRACT .....	iii
SUMMARY .....	iv
I. INTRODUCTION .....	1
II. EXPERIMENT CONFIGURATION AND TEST CONDUCT .....	5
1. FUEL ROD AND TEST HARDWARE .....	5
2. POWER HISTORY .....	5
3. RESULTS FROM ON-LINE MEASUREMENTS .....	8
III. EFFECTS OF FILM BOILING ON OPERATION OF FAILED FUEL ROD .....	13
1. OVERALL FUEL ROD APPEARANCE .....	13
2. CLADDING FAILURE MECHANISM AND BREAKUP .....	13
3. FUEL FAILURE MECHANISMS AND BREAKUP .....	19
IV. FUEL ROD TEMPERATURE PROFILE .....	20
1. AXIAL PROFILE .....	20
2. CIRCUMFERENTIAL PROFILE .....	23
3. RADIAL PROFILE .....	26
V. CLADDING CHEMICAL REACTIONS .....	29
1. FUEL-CLADDING REACTION .....	29
2. CLADDING-COOLANT REACTION .....	32
3. CLADDING EMBRITTLEMENT .....	34
4. CLADDING HYDRIDING .....	38
VI. FUEL RESTRUCTURING .....	43
1. POROSITY CHANGES .....	43
2. FUEL MELTING .....	45
3. FUEL SHATTERING .....	45
4. EQUIAXED GRAIN GROWTH .....	50
5. CHEMICAL CHANGES .....	51

VII. CONCLUSIONS .....	55
VIII. REFERENCES .....	56
APPENDIX A — PRETEST FUEL ROD AND SHROUD CHARACTERISTICS AND INSTRUMENTATION .....	59
APPENDIX B — TEST ROD POWER PROFILE .....	69
APPENDIX C — METALLOGRAPHIC EXAMINATION .....	79
APPENDIX D — PARTICLE SIZE ANALYSIS .....	87
APPENDIX E — MICROPROBE EXAMINATION .....	93
APPENDIX F — CLADDING THERMAL CONDUCTIVITY CHANGES .....	103
APPENDIX G — UO <sub>2</sub> OXIDATION CALCULATION .....	107

## FIGURES

1. Test PCM-1 fuel rod and test train configuration .....	6
2. Fuel rod peak power as a function of time for Test PCM-1 .....	8
3. Coolant pressure, flow rate, inlet temperature, and rod peak power for the DNB portion of Test PCM-1 .....	9
4. Fuel rod peak power, plenum pressure, and elongation for the DNB portion of Test PCM-1 .....	10
5. Cladding surface temperatures at the 0.58-, 0.68-, and 0.78-m elevations for the DNB portion of Test PCM-1 .....	11
6. Overall view of Test PCM-1 fuel rod .....	14
7. Overall view of broken cladding sections .....	15
8. Cross sections of broken cladding .....	17
9. Overall view of surface roughness in oxide on the inner surface of the shroud at high power region .....	18
10. Axial progression of film boiling from thermocouple response data .....	21
11. Cladding axial temperature profile from posttest microstructures .....	23
12. Isometric plot of the isothermal effective cladding temperature as a function of angular orientation and axial position .....	24
13. Cladding microstructures at 0.67 m showing circumferential temperature gradient .....	25



14. Fuel rod radial temperature profile at 0.30 and 0.67 m .....	28
15. Several orientations of the cladding at 0.67 m showing typical zircaloy-UO <sub>2</sub> , zircaloy-steam interactions .....	30
16. Uranium distribution in the inner oxide layer at several orientations of the 0.30-m elevation .....	31
17. Uranium distribution in the oxidized cladding at 0.59 and 0.52 m .....	33
18. Examples of totally oxidized cladding .....	35
19. Cladding at 0.30 m showing progressively greater extent of oxidation and less melting .....	36
20. Zirconium-oxygen equilibrium phase diagram .....	37
21. Cladding microhardnesses at 0.67 and 0.74 m .....	39
22. Cladding microhardnesses at 0.30 and 0.52 m .....	40
23. Hydriding in the zircaloy cladding near the top of the film boiling zone .....	41
24. Fuel porosity at several elevations .....	44
25. Cross sections of all examined fuel surfaces .....	46
26. Molten fuel radii .....	48
27. Fuel shattering at 0.67 and 0.74 m .....	49
28. Uranium-oxygen equilibrium phase diagram .....	52
29. Fuel structures at several elevations showing U <sub>4</sub> O <sub>9</sub> precipitates .....	53
30. Fuel structure at 0.30 m .....	54
A-1. Illustration of PCM-1 test assembly showing the relative locations of the fuel rod instrumentation .....	65
A-2. Photographs of upper and lower flow shroud screens .....	66
A-3. Schematic of upper and lower flow shroud screens .....	67
B-1. Test PCM-1 normalized flux wire profile .....	77
C-1. Beta-gamma autoradiographs of mounted samples .....	85
E-1. Microprobe trace of cladding at 95 and 290 degrees, and fuel and cladding at 225 degrees; 0.30-m elevation .....	96
E-2. Microprobe trace of cladding at 125, 165, 210, and 235 degrees; 0.30-m elevation .....	97
E-3. Microprobe trace of cladding and fuel at 260 and 335 degrees; 0.52-m elevation .....	99

E-4. Microprobe trace of cladding and fuel at 90, 130, and 225 degrees; 0.52-m elevation .....	100
E-5. Microprobe trace of cladding and fuel at 0, 90, 120, and 180 degrees; 0.59-m elevation .....	101
E-6. Microprobe trace of cladding and fuel at 0, 90, 180, and 270 degrees; 0.67-m elevation .....	102

## TABLES

I. Categories of Post-DNB Fuel Behavior During a PCM Event .....	2
II. PCM Test Program .....	3
III. Summary of Test PCM-1 Test Conditions .....	7
IV. Calculated Effective Isothermal Temperatures .....	22
V. Molten Fuel Radii Data .....	27
VI. Equiaxed Grain Growth .....	50
A-I. Test PCM-1 Fuel Rod Component Pretest Data .....	62
A-II. Pellet Characterization Data for Test PCM-1 Fuel Rod .....	63
B-I. Radiochemical Analysis Results .....	72
B-II. Flux Wire Gamma Scan Data .....	73
C-I. Sectioning Schedule for Test PCM-1 Fuel Rod .....	82
D-I. Fuel Rod Inventory .....	89
D-II. Fuel Particle Size Distribution .....	90
D-III. Cladding Particle Size Distribution .....	90
D-IV. Particle Size Distribution of Debris from Top and Bottom Flow Shroud Screens .....	91
F-I. Cladding Thermal Conductivity Change .....	106

# FUEL ROD MATERIAL BEHAVIOR DURING TEST PCM-1

## I. INTRODUCTION

Projected growth of the nuclear power industry in the United States requires continuing investigation of the likelihood and consequences of potential reactor accidents in order to better quantify their potential effects on public health and safety. Essentially all such postulated accidents involving the cores of light water reactors (LWRs) are due to an imbalance between the heat generation rate in the fuel and the heat removal capacity of the coolant. The extreme cases have traditionally been designated as the loss-of-coolant accident, in which part or all of the core coolant is lost, and the reactivity initiated accident, in which there is a sudden severe increase in power due to the ejection of a control rod. Between these two extremes, LWR accidents resulting in off-normal power-cooling conditions are generally termed power-cooling-mismatch (PCM) accidents. Numerous credible, single and coincident initiating events that may lead to PCM accidents can be postulated. For example, overpower events can result from malpositioned or unplanned withdrawal of control rods, xenon instability, loading and operation of a fuel assembly in an improper location (enrichment error), decreases in the reactor coolant soluble poison concentration, increased reactor coolant flow rate, or low temperature of the inlet coolant caused by startup of an inactive loop at an incorrect temperature. Undercooling can be caused, for example, by a spectrum of coolant flow reduction incidents resulting from various primary pump malfunctions or electrical power losses, localized flow blockages, or secondary system malfunctions that result in increased or decreased heat removal from the primary coolant system. If departure from nucleate boiling occurs during a PCM event, fuel rod damage and subsequent release of radioactivity into the primary system may occur.

The Power-Cooling-Mismatch Test Series is being conducted by the Thermal Fuels Behavior Program of EG&G Idaho, Inc., as part of the U.S. Nuclear Regulatory Commission's Fuel Behavior Program<sup>1</sup>. These tests are being performed to characterize the behavior of unirradiated pressurized water reactor (PWR) type fuel rods at power densities and flow conditions ranging from normal operating conditions to beyond the occurrence of departure from nucleate boiling (DNB)<sup>2</sup>. The test series is directed toward providing an experimental data base to satisfy one of the major objectives of the Fuel Behavior Program — the development of verified analytical models of fuel rod behavior during normal and off-normal operating conditions.

Four categories of possible post-DNB fuel rod behavior during a PCM event have been identified, as shown in Table I. The physical processes which determine the particular category of expected post-DNB fuel rod behavior during a PCM event are zircaloy phase changes, the degree of zircaloy-water and zircaloy-fuel reaction (both of which influence cladding ductility), and fuel melting. The principal variables that control these processes are cladding temperature, the time at temperature, and rod power. The PCM Test Series was designed as a parametric evaluation of fuel rod behavior response during film boiling, with cladding temperature, time in stable film boiling, and rod power being the primary variables, as outlined in Table II.

This report presents the fuel rod materials behavior results of Test PCM-1, the final single-rod test in the PCM Test Series being conducted in the Power Burst Facility (PBF) at the Idaho National Engineering Laboratory, and is based on the postirradiation examination. The fuel rod test response is discussed in the Test PCM-1 Fuel Rod Behavior Report<sup>3</sup>. The test objectives were (a) to determine the time to failure of a single PWR-type fuel rod subjected to film boiling operation at high power, (b) investigate the mechanism of rod failure, (c) examine any evidence of energetic molten fuel-coolant interaction and molten fuel related rod failures, and (d) evaluate the behavior of a rod subjected to film boiling operation at high

TABLE I

CATEGORIES OF POST-DNB FUEL BEHAVIOR DURING A PCM EVENT

Category	Cladding Temperature Range (K)	Zircaloy Cladding Phase	Zircaloy/Water Reaction	Cladding Ductility	Potential Fuel Rod Failure Modes
1	<810	$\alpha$	None	Normal	None for unirradiated fuel rods.
2	810 to 1105	$\alpha$	None	High	Large deformations <sup>a</sup> to rupture <sup>a</sup> ; fuel melting.
3	1105 to 1245 <sup>b</sup>	$\alpha + \beta$	Minimal	Low	Small deformations to rupture <sup>a</sup> ; fuel melting.
4	>1245	$\beta$	Severe	High to low <sup>c</sup>	Cladding oxidation and oxygen embrittlement. Fuel melting if powers are relatively high.

a. Cladding ballooning is unlikely and is possible only after the internal rod pressure exceeds the system pressure.

b. This temperature range bounds the cladding ductility minimum that occurs near the middle of the  $\alpha + \beta$  two-phase region.

c. The cladding ductility is initially high in  $\beta$ -zircaloy, but decreases rapidly as the zircaloy is embrittled by oxidation and oxygen absorption.

TABLE II

## PCM TEST PROGRAM

Test Parameters	Test						
	PCM-1	PCM-2A	PCM-2	PCM-3	PCM-4	PCM-5	PCM-7a
Number of test rods	1	1	4 <sup>b</sup>	4 <sup>b</sup>	4 <sup>b</sup>	9	9
Target maximum cladding temperature	>1245	810 to 1105	810 to 1105	1105 to 1245	>1245	>1245	>1245
Maximum time of stable film boiling (s)	900	210	117	60	160	660	~660
Maximum linear peak power (kW/m)	78	58	51	54	68	56	58
Number of DNB cycles	1	9	8	5	5	1	3
Coolant inlet temperature (K)	605	600	600	600	600	590	605

a. Test PCM-6 was deleted from the program.

b. Four test rods situated in a square array with individual flow shrouds.

power following rod failure. The test was conducted at a power level above the upper limit of the fuel rod powers anticipated for postulated PCM events. The specific objectives of this report are to present (a) the analysis of the effects of film boiling operation on fuel and cladding failure and subsequent breakup, and (b) the investigation of the interaction of the fuel, cladding, and coolant, as well as the estimated fuel rod temperature distribution.

The Test PCM-1 fuel rod was contained in a circular flow shroud and positioned within the PBF in-pile tube (IPT). Coolant conditions (pressure and inlet temperature) typical of a PWR were maintained in the IPT throughout the nuclear testing. The nuclear portion of the test consisted of power calibration, test rod preconditioning, and DNB or film boiling operation. The DNB operation was initiated by rapidly increasing test rod peak power to 69 kW/m at constant coolant conditions. A description of the experiment configuration, power history, and test thermal-hydraulic conditions as determined by on-line measurements is presented in Section II. Details of the test rod parameters and instrumentation used in the test are discussed. A summary of the on-line measurements is presented.

Observations of the effects of film boiling on the operation of a failed fuel rod are presented in Section III. The overall appearance and gross damage to the test rod are discussed. The initial rod failure and subsequent breakup are evaluated.

Fuel rod radial, and the cladding axial and circumferential temperature distributions as determined from fuel and cladding microstructures and reaction layer thicknesses are discussed in Section IV.

Chemical reactions from cladding-steam and cladding-fuel interactions are discussed in Section V. The cladding embrittlement from oxidation is assessed and the influence of hydrogen pickup on cladding microstructure and microhardness is discussed.

Fuel restructuring information, specifically fuel melting and grain growth characteristics, porosity changes, and the effects of the chemical interaction of the fuel with the cladding and coolant on these phenomena, are presented in Section VI.

The detailed data from the postirradiation examination and pretest characterization are provided in Appendices A through G. (All of the appendices to this report are presented on microfiche attached to the inside of the back cover.) The as-built fuel rod and shroud characterization data and instrumentation are contained in Appendix A. A description of the axial power profile is presented in Appendix B. Additional metallography illustrating the physical and chemical changes in the cladding and fuel is presented in Appendix C. Data from the particle size analysis of the broken fuel rod pieces are tabulated in Appendix D. Appendix E contains the details of the microprobe examination. The changes in cladding thermal conductivity with oxidation to  $ZrO_2$  are discussed in Appendix F. The  $UO_2$  oxidation calculation is presented in Appendix G.

## II. EXPERIMENT CONFIGURATION AND TEST CONDUCT

Test PCM-1 was performed in the PBF in-pile test loop. The PBF driver core test space is designed to operate as a neutron flux trap which permits high power densities in tested fuel rods relative to the active core power density. The fuel rod and test hardware, power history, and results from on-line measurements are summarized in this section.

### 1. FUEL ROD AND TEST HARDWARE

The fuel rod was composed of a 0.91-m-long fuel stack of 20% U-235 enriched uranium dioxide ceramic fuel pellets contained in a zircaloy-4 cladding tube with an outside diameter of 10.72 mm and a wall thickness of 0.61 mm. Other pretest characterization data are presented in Appendix A. All elevations given are referenced to the bottom of the fuel stack unless otherwise stated. The nominal distance from the bottom of the fuel rod to the bottom of the fuel stack was 24.13 mm. During testing, the fuel rod was rigidly fixed at the top end cap in a 16.3-mm inner diameter flow shroud and was free to expand axially downward onto a length change transducer. The flow shroud directed the coolant upwards over the fuel rod and effectively thermally and hydraulically isolated the rod. The rod shroud was centered in the PBF in-pile tube and was fitted at both ends with particle screens specified to have minimum openings of 25 to 50  $\mu\text{m}$  and tested to be less than 76  $\mu\text{m}$ . Details of shroud screens are given in Appendix A. A cut-away schematic of the PCM-1 fuel rod and the test train configuration is shown in Figure 1.

The fuel rod was instrumented for the measurement of the internal gas pressure, cladding surface temperature, and fuel rod axial elongation. The test assembly was instrumented for measurement of the coolant pressure, coolant temperature, coolant flow rate, and local neutron flux for use in power calibration and thermal-hydraulic test analysis. A detailed description of the fuel rod and test train instrumentation is also given in Appendix A.

### 2. POWER HISTORY

Nuclear operation during Test PCM-1 included a power calibration period, a preconditioning period, and the DNB or film boiling portion of the test. The test conditions for each phase are given in Table III. The fuel rod peak power for the entire test is plotted in Figure 2. The fuel rod axial power profile is presented in Appendix B. The purpose of the power calibration phase was to determine the test rod power with respect to the self-powered neutron detector (SPND) current. Test rod powers were determined at several core power levels at nominal coolant conditions of 595 K inlet temperature, 4400  $\text{kg/s} \cdot \text{m}^2$  mass flow rate, and 15.3 MPa pressure. The maximum fuel rod peak power during this phase was 46  $\text{kW/m}$ .

The preconditioning phase of the test provided an operation history sufficient to allow fuel pellet cracking and relocation. The cladding surface was aged to reduce the possibility of premature DNB occurring due to outgassing<sup>4</sup>. The preconditioning period also served to establish a fission product inventory within the test rod which allowed detection of rod failure as well as the approximate time of the failure. The inlet temperature averaged 593 K, with a system pressure of 15.3 MPa, and the mass flow rate varied from 1232 to 4400  $\text{kg/s} \cdot \text{m}^2$ . The maximum fuel rod peak power during this phase was 50  $\text{kW/m}$ .

The film boiling portion of the test provided information on fuel rod behavior in the film boiling heat transfer regime. Departure from nucleate boiling was initiated by rapidly increasing test rod power at constant coolant conditions from a peak power of 38  $\text{kW/m}$ , at which equilibrium conditions were established, to a peak power of 69  $\text{kW/m}$  at a rate of 20  $\text{kW/m}$ . The test rod was held at these nominal conditions until approximately 280 seconds after the beginning of the initial power ramp. The test rod peak power was then increased to 78  $\text{kW/m}$  and held for approximately 640 seconds. There was an indication of rod failure at approximately 520 seconds from the start of the first power ramp. The coolant flow rate through the rod shroud was increased at the time of reactor scram to cool the test rod. The rod shroud coolant flow rate decreased rapidly 25 seconds after scram due to an apparent flow blockage. The coolant inlet temperature averaged 600 K, with a system pressure of 15.2 MPa. The coolant flow rate varied from 980 to 1170  $\text{kg/s} \cdot \text{m}^2$  during film boiling operation.

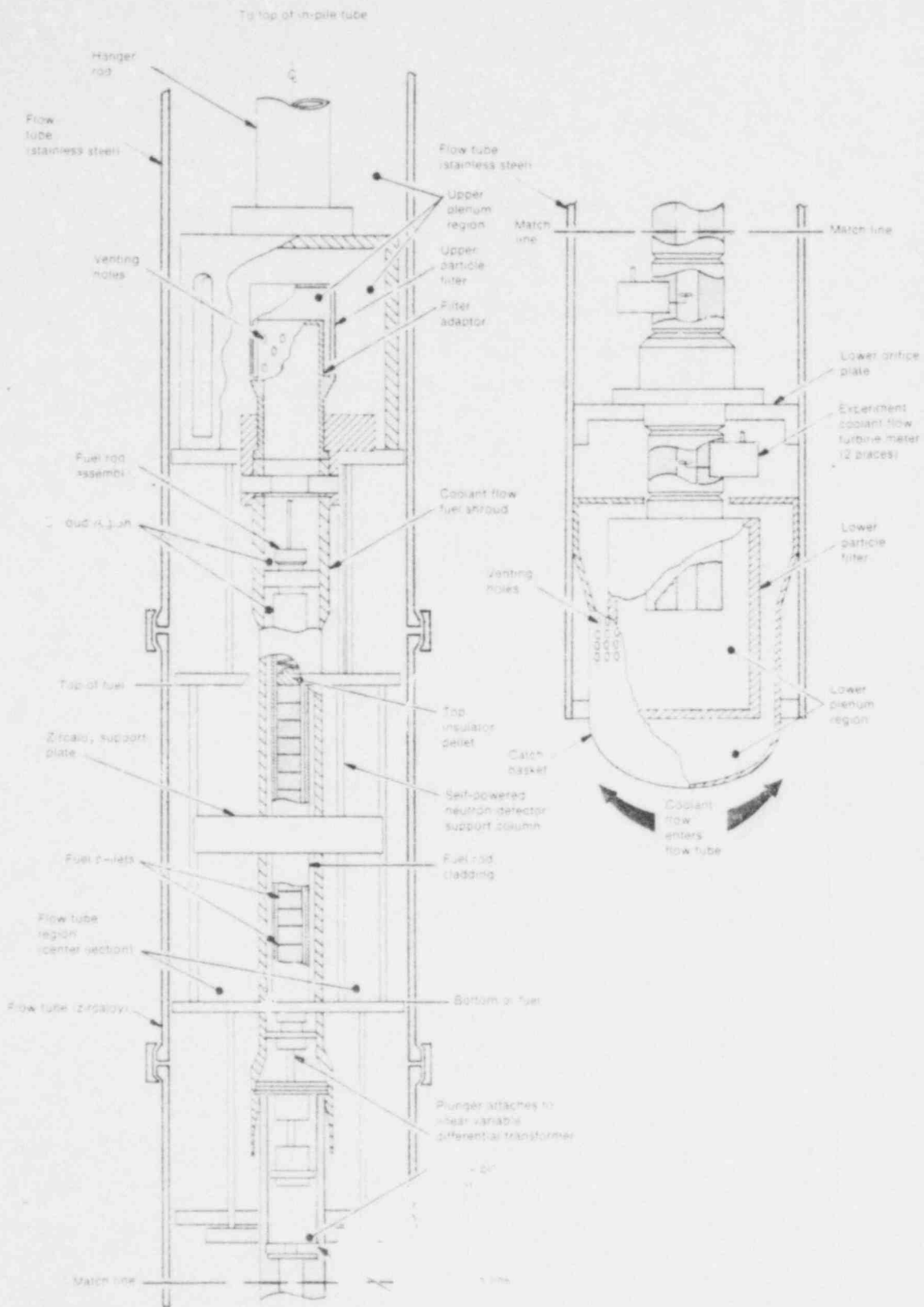


Fig. 1 PCM-1 fuel rod and exit train assembly.



TABLE III

## SUMMARY OF TEST PCM-1 TEST CONDITIONS

	Approximate Time (min)	Indicated Reactor Power (MW)	Test Rod Peak Power <sup>a,b</sup> (kW/m)	Coolant Flow Rate (kg/s m <sup>2</sup> )	Inlet Temperature (K)	Coolant $\Delta T$ (K)	System Pressure (MPa)
Power	30.0	0.1	0.27	4480	591	0.21	15.34
Calibration	68.8	2.0	12.32	4416	594	2.43	15.38
Phase	19.2	4.5	28.26	4396	596	5.44	15.39
	21.3	6.0	35.91	4403	595	6.87	15.35
	9.5	8.0	46.07	4361	596	8.74	15.31
	13.0	10.0	57.15	4313	597	10.76	15.32
	15.8	6.0	36.56	4412	596	6.94	15.31
	11.8	4.5	27.49	4401	595	5.30	15.29
	11.0	0.1	0.28	4417	594	0.15	15.31
Preconditioning	13.0	0.1	0.38	4272	591	0.08	15.14
Phase	2.5	5.0	27.30	4400	595	5.30	15.30
	21.3	1.5	10.30	4174	595	2.12	15.15
	61.9	5.1	31.68	4088	596	6.43	15.17
	5.0	0.1	3.41	4080	595	0.72	15.23
	10.0	7.0	42.75	3202	595	11.02	15.20
	55.0	7.0	42.36	1797	594	c	15.28
	4.0	0.1	0.45	1840	589	0.21	15.24
	59.1	9.0	50.13	1796	595	c	15.27
	10.6	0.1	0.22	1501	587	0.14	15.22
	30.3	6.0	35.77	1232	591	c	15.43
	7.0	0.1	0.35	2253	587	0.15	15.38
DNB	4.0	0.1	0.51	1170	591	-	15.18
Phase	41.0	6.4	38.60	1188	597	c	15.22
	3.3	11.5	69.34	1110	603	c	15.27
	2.6	12.6	75.62	1052	605	c	15.21
	2.1	12.8	76.57	980	606	c	15.25
	6.1	13.0	77.80	1087	605	c	15.25

a. Rod power was determined by regression of the self-powered neutron detectors.

b. Test rod peak power is based on a peak-to-average ratio of 1.365.

c.  $\Delta T$  measurement unreliable due to saturated outlet coolant conditions.

631  
170

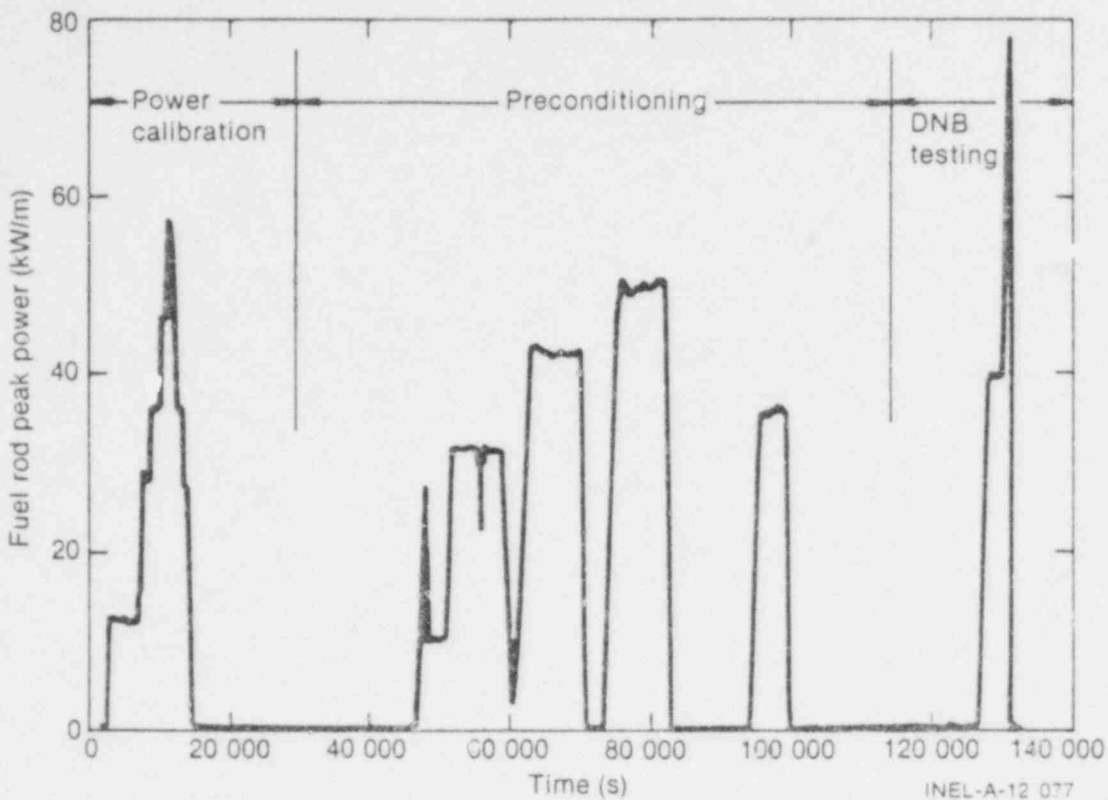


Fig. 2 Fuel rod peak power as a function of time for Test PCM-1.

### 3. RESULTS FROM ON-LINE MEASUREMENTS

The PCM-1 test train was instrumented to measure coolant and fuel rod conditions. The summary of the on-line measurements presented in this section will be referred to later for confirmation of analyses of fuel rod failure mechanisms and breakup made from posttest evidence. The coolant flow rate, inlet temperature, and system pressure used in the film boiling phase are illustrated in Figure 3. Fuel rod internal pressure and fuel rod elongation response are shown in Figure 4. These two plots include rod peak power for comparison. The measured cladding surface temperature is plotted for three locations in Figure 5. On all of the plots, zero time is the beginning of the power ramp for the film boiling phase<sup>5</sup>.

The coolant flow rate decreased slightly through the first 540 seconds of film boiling. The flow rate was increased twice, at 600 and 800 seconds, to bring it up to the original value. At the time of the reactor scram the flow rate was increased to cool the test rod. A decrease to 20% of the original flow occurred 25 seconds after scram and was probably associated with a partial flow blockage. The coolant inlet temperature, originally 591 K, gradually increased during film boiling, reaching 606 K near the end of the DNB phase. The system pressure was constant throughout the test, except for a 0.3 MPa increase following the shutdown. This system pressure increase was probably associated with the pump pressure change necessary to increase the coolant flow rate.

The fuel rod internal pressure increased during the first 60 seconds of film boiling in response to the higher fuel temperature. There was no change in internal pressure throughout the rest of the nuclear operation. The pressure started to drop with rod cooling at the reactor scram but communication between the rod plenum and the coolant occurred and the rod pressure rose to the system pressure. The linear variable differential transformer (LVDT) indicated a rod length increase at DNB. There was a decrease in length between 400 and 500 seconds, followed by two increases in length: one at 520 seconds and one at

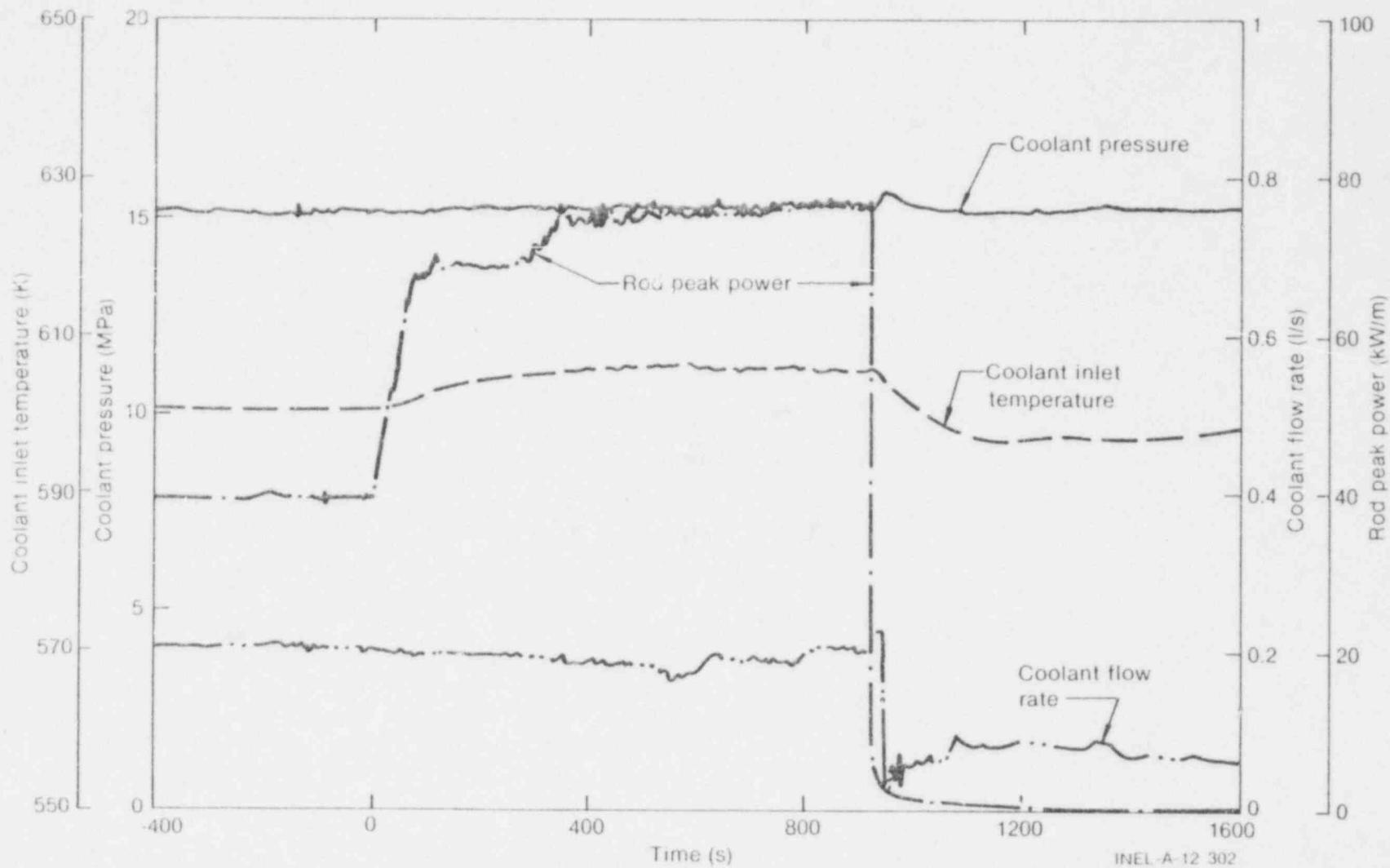


Fig. 3 Coolant pressure, flow rate, inlet temperature, and rod peak power for the DNB portion of Test PCM-1.

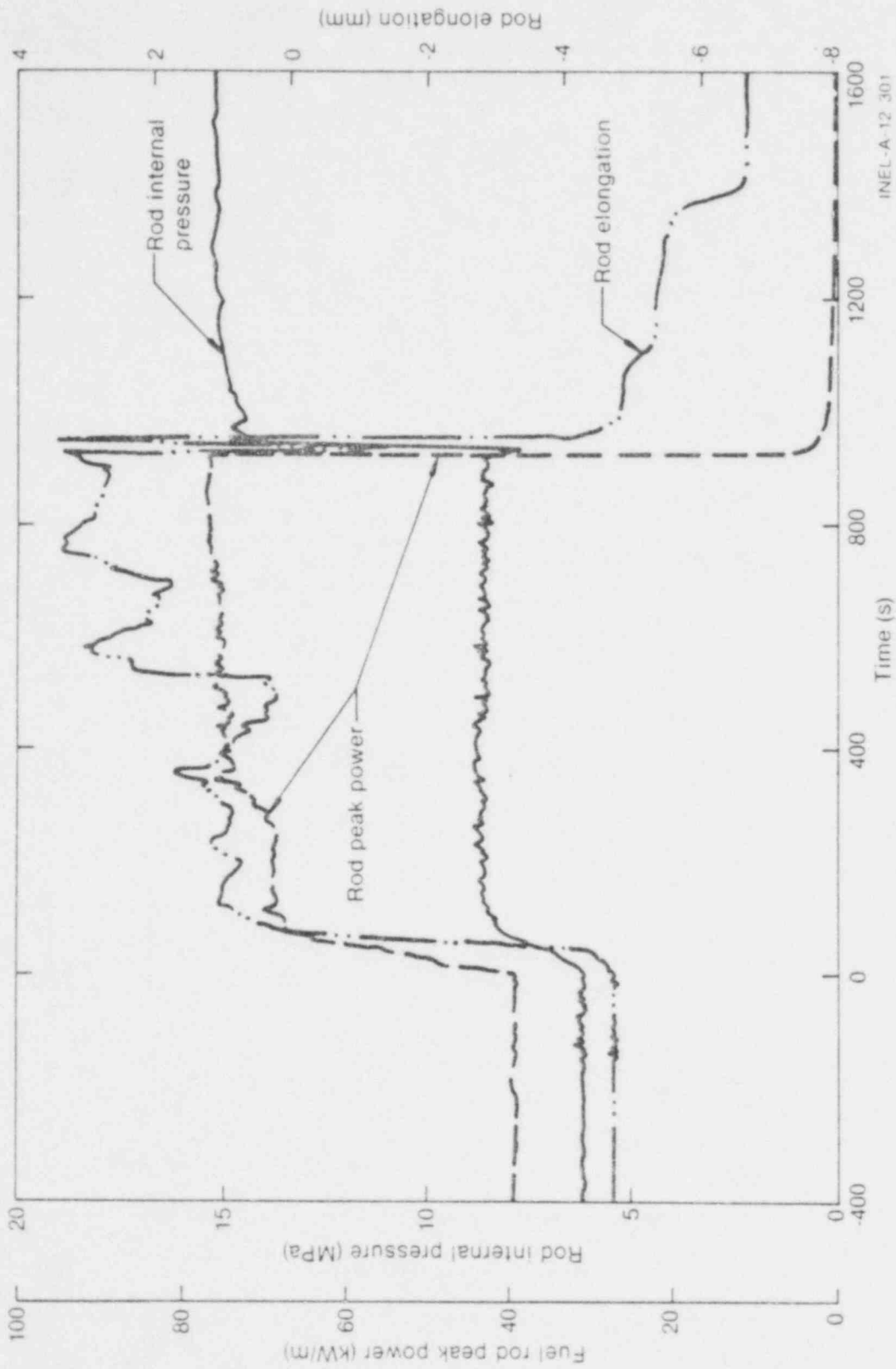


Fig. 4 Fuel rod peak power, plenum pressure, and elongation for the DNB portion of TEST PCM-1.

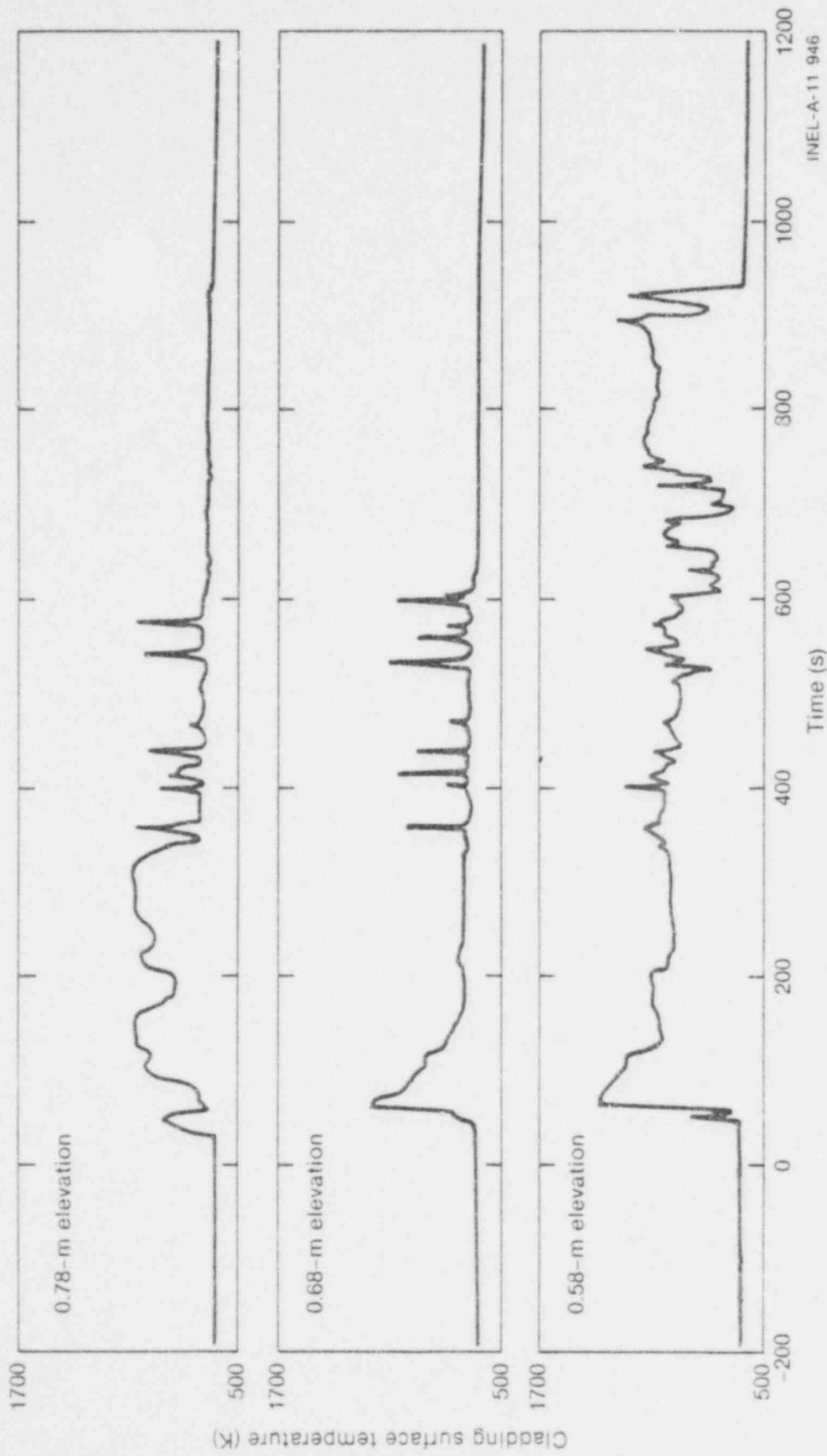


Fig. 5 Cladding surface temperature for the 0.58, 0.68, and 0.78 elevation for the DNB portion of Test PCM-1.

700 seconds. A large decrease in rod length occurred during the reactor scram, indicating severe rod breakup. A remote area radiation monitor showed a stepwise increase from normal background to full scale at approximately 600 seconds after the start of the power ramp, indicating rod failure. The fission product detection system (FPDS)<sup>6</sup> response increased two orders of magnitude at 637 seconds in the DNB phase. After reactor scram the system showed another large increase, suggesting additional rod breakup. Previous testing of fuel rods having experienced radical PCM conditions has shown that highly embrittled test rods will fail almost immediately upon rewet from film boiling conditions. The FPDS response following reactor shutdown therefore set the delay time of the system at approximately 105 seconds. The 'at power' delay time, obtained from the relative flow rates during operation, was found to be approximately 118 seconds, therefore indicating rod failure at 519 seconds.

All of the cladding thermocouples performed erratically during the DNB portion of the test. The 0.53-m thermocouple failed during the initial transient and results are not presented here. Each of the thermocouples may have formed one or more new junctions later in the test. The thermocouple response data are used in this report to determine the initiation of film boiling.

### III. EFFECTS OF FILM BOILING ON OPERATION OF A FAILED FUEL ROD

The primary objective of Test PCM-1 was to evaluate the behavior of a single fuel rod subjected to film boiling operation at high power following rod failure. The posttest appearance of the fuel rod can give clues as to the failure mechanisms and the response of fuel rod components to film boiling operation after rod failure. The overall posttest appearance of the fuel rod is described, and possible fuel and cladding failure mechanisms and rod breakup are discussed in the following subsections. Gross interactions of the fuel rod with the flow shroud and coolant are also evaluated. The detailed fuel and cladding information necessary for the analysis of the overall rod failure mechanisms and breakup is given in Sections IV, V, and VI.

Significant breakup of the Test PCM-1 fuel rod occurred during the test. Posttest examination revealed a large fraction of the fuel stack was washed through the flow shroud particle screens. It is important to determine the time during the test that rod breakup occurred. Fuel rod failure during high power operation may be a more critical safety consideration in terms of loss of coolable geometry and release of fuel and fission products to the coolant than loss of cladding integrity and breakup of the fuel at shutdown.

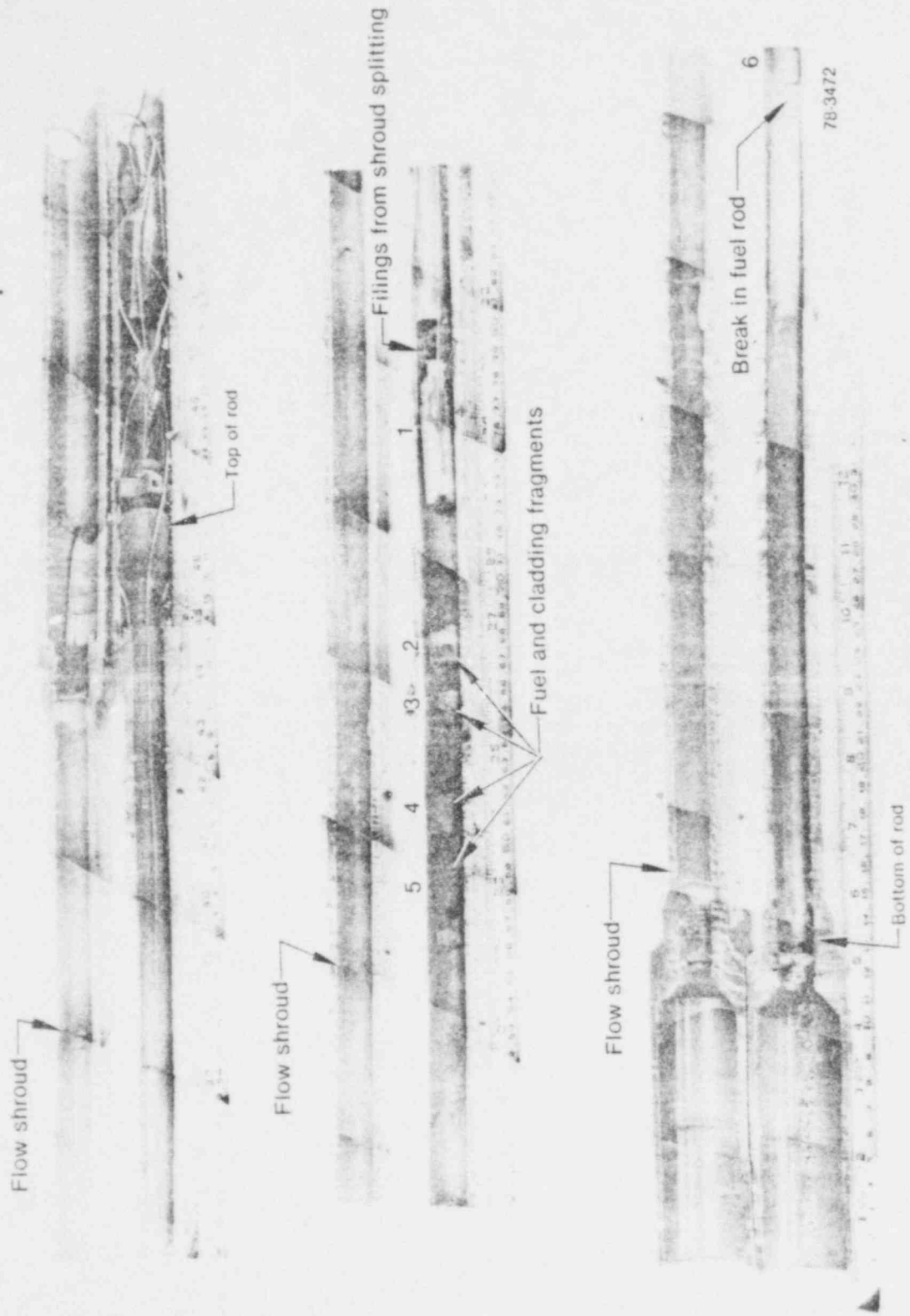
#### 1. OVERALL FUEL ROD APPEARANCE

The Test PCM-1 fuel rod was initially examined to identify and document the overall posttest condition of the rod. The flow shroud was split longitudinally and opened up to expose the fuel rod. The split shroud with the failed fuel rod and a scale, indicating distances from the bottom of the shroud, are shown in Figure 6. The broken pieces of fuel rod are numbered in the photograph for identification purposes. The debris in the bottom enlarged portion of the shroud is filings from the splitting operation. Broken pieces of cladding lying around the bottom end cap are illustrated in Figure 7(a). Very few fuel pieces are seen at this location. The lower film boiling boundary is located at 0.35 m on the scale in Figure 6 (0.21 m from the bottom of the fuel stack), as indicated by the change from a dark to a light oxide. A thin white deposit on the inside surface of the shroud matching the pattern of the white oxide on the cladding is also shown. A major break in the rod occurred at 0.44 m (0.30 m from the bottom of the fuel stack). Above this location are six loose fuel pieces without cladding, one of which is almost two pellet lengths long. Two pieces with cladding partially intact, and a 0.06-m section with the entire cladding intact are located above the fuel pieces. At 0.77 m, a section of cladding is attached to a thermocouple sheath at a braze. The cladding piece has been raised off of the fuel. Figure 7(b) shows a side view of this cladding fragment. Additional cutting debris observed between 0.79 to 0.80 m is a result of the splitting operation. The fuel rod to shroud spacing does not permit the interchange of fuel rod pieces, and although some axial movement of the pieces may have taken place, the loose pieces of fuel rod are assumed to be at their operating locations within the flow shroud.

The top intact portion of the rod begins at 0.80 m (0.63 m from the bottom of the fuel stack), and is positioned in its original axial location in the shroud (the rod was rigidly fixed at the top end cap). The bottom section of rod dropped 28 mm in the shroud. Cladding collapse at the pellet interfaces occurred from 0.80 to 0.96 m (0.63 to 0.79 m from the bottom of the fuel stack). The upper film boiling boundary is at approximately 1.02 m (0.85 m from the bottom of the fuel stack).

#### 2. CLADDING FAILURE MECHANISM AND BREAKUP

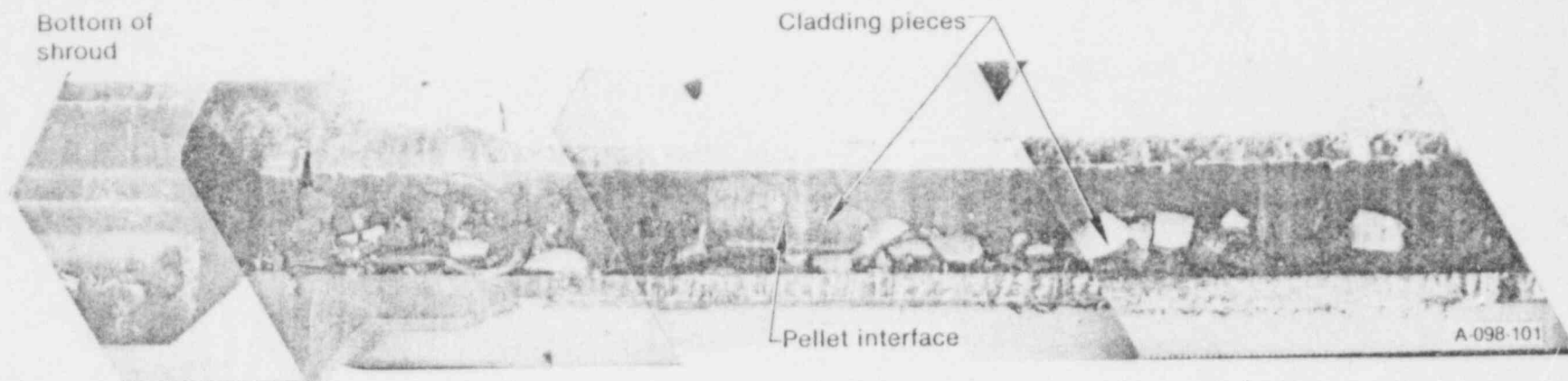
The exact sequence of events during the failure and subsequent operation in film boiling of the Test PCM-1 rod is difficult to determine from the posttest evidence alone due to the extensive chemical and mechanical interaction of the fuel rod components. The fission product detection system indicated rod failure at about 517 seconds, using a calculated delay time of approximately 120 seconds. An increase in rod length measured by the LVDT at 520 seconds corresponds to the increase in the fission product activity, and therefore fixes the time of initial rod failure at about 520 seconds. Another large increase in



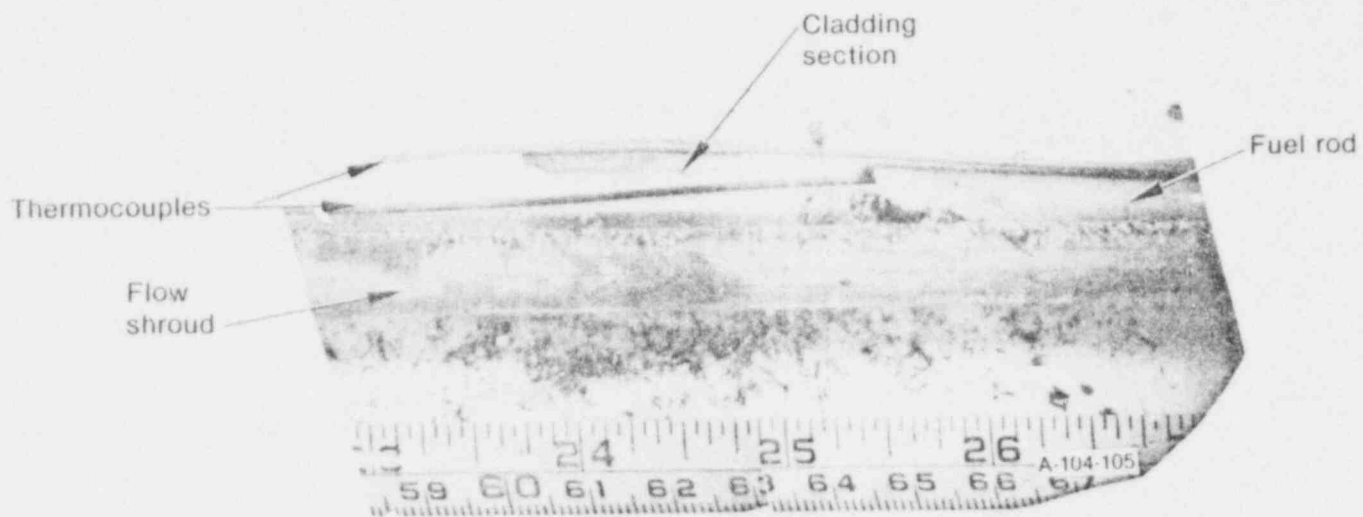
GS-011-25

Fig. 6 Overall view of Test PCM-1 fuel rod.





(a) Debris from around bottom end cap



(b) Cladding section attached to thermocouple

GS-011-26

Fig. 7 Overall view of broken cladding sections.

15  
631 178

radioactivity indicated by the FPDS occurred at shutdown, along with a decrease in rod length and coolant flow. Postirradiation examination suggests that extensive cladding breakup occurred before shutdown, probably beginning at 520 seconds, and additional rod breakup and blockage of the flow through the shroud occurred at shutdown.

The initial failure mechanism was cladding embrittlement. The calculations in Subsection V-2 show that the cladding was embrittled after 515 seconds of film boiling operation. The strain that the thermally expanded fuel placed on the embrittled cladding may have been sufficient to initiate failure. The location of the initial failure cannot be determined.

Large pieces of cladding were found near the bottom and top end caps. The several broken pieces examined metallographically were found to be only partially oxidized. Cross sections of some of the pieces examined are shown in Figure 8. The unoxidized fracture surfaces suggest that either the pieces fell into the coolant stream and out of the steam envelope immediately after fracture and prior to complete oxidation, or the pieces fractured after test shutdown. The pieces are from the center section of rod that is missing, probably toward the lower end. After the initial failure at an embrittled location, the bottom portion of rod may have been separated from the top. Repeated contact of the loose portion of the rod with the shroud could have resulted in breakup of cladding that was not completely embrittled. Cross sections of cladding from intact portions on each side of the high power (middle) region of the rod show cladding oxidation through the entire wall. On the basis of the extent of cladding oxidation in the lower power regions, the cladding in the high power region would have completely oxidized had it remained intact. Therefore, the loose pieces of cladding from the high power region must have broken off at some point during the test, before oxidation of the cladding was complete.

There were indications in the fuel of extensive cladding breakup during film boiling operation. The fuel rod sections with no intact cladding were from the high power region. These sections had smaller melt radii and, therefore, lower surface temperatures than locations at lower power regions with cladding still intact. After cladding in the high power region broke away, oxidation of the intact cladding at the lower power regions continued, insulating the fuel and raising the fuel temperature. Therefore, the lower power regions of the rod with oxidized cladding intact operated with higher fuel temperatures than the unclad sections from the high power region. (The temperature difference between clad and unclad fuel pellets is discussed further in Subsection VI-2.)

The mechanics of the cladding breakup are not easily explained. All of the cladding through the film boiling region was embrittled and could have failed. However, only cladding in the highest power region fragmented. Possibly, at the time of the initial failure, the higher fuel temperatures in the high power region created greater thermal expansion of the fuel and, therefore, more strain on the cladding. The pieces of cladding remaining in the shroud as debris do not account for all of the missing cladding. Some of the cladding may have broken up due to thermal shock at shutdown. Since the cladding would have been completely oxidized at that time, it probably powdered and was swept away in the coolant stream through the particle screens. At regions where the cladding was not completely oxidized, some of the oxide layers that formed spalled off. It is likely that the spalled oxide also powdered and was swept through the screens.

A thin grey oxide coated the inside of the flow shroud, with a slight discoloration in the oxide corresponding to the oxide pattern on the fuel rod at the lower end of the film boiling zone. Some roughness existed in the flow shroud oxide corresponding to the high power region of the fuel rod. An example of this area is shown in Figure 9. Some of the roughness may be due to spattering or condensation of molten fuel. The oxide and deposits were so thin that a sample could not be scraped off to determine the exact compositions by X-ray diffraction analysis.

The matching oxide patterns on the inside of the shroud and the outside of the fuel rod indicate that the rod broke into two pieces and the bottom section slid down 28 mm. The rod then remained in this failed configuration. The time at which the bottom portion of the rod slid down could not be determined from the rod length change response and, therefore, probably did not occur during testing. Possibly, the rod section slid down after shutdown and the oxide pattern is due to evaporation of the water remaining in the shroud while the fuel rod was lying against it.

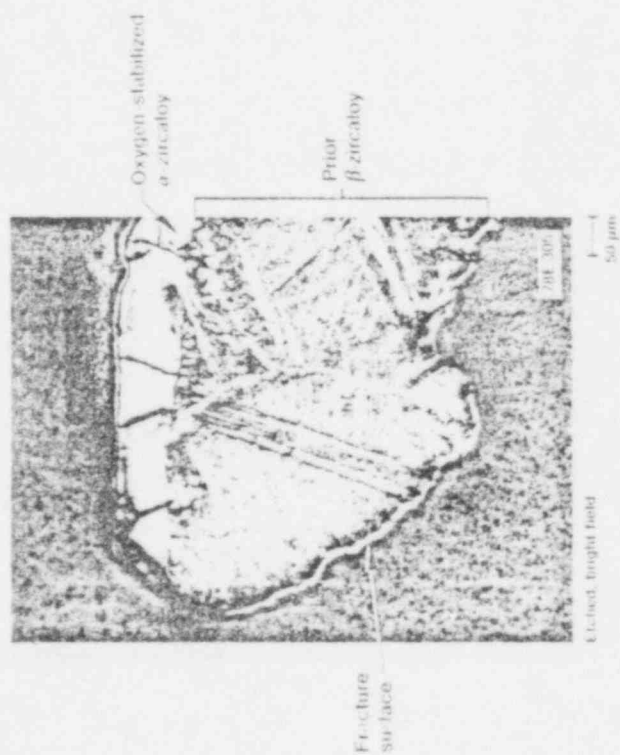
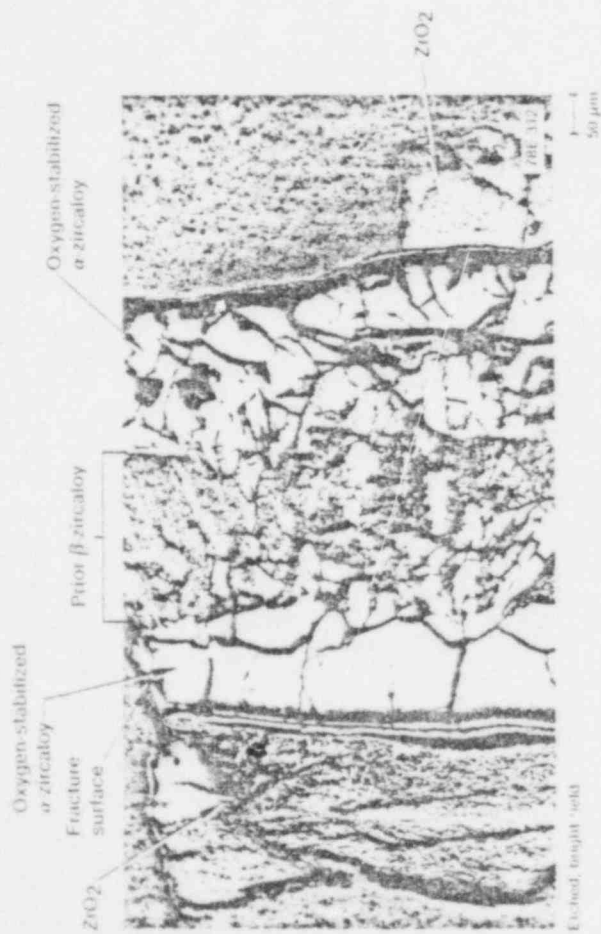
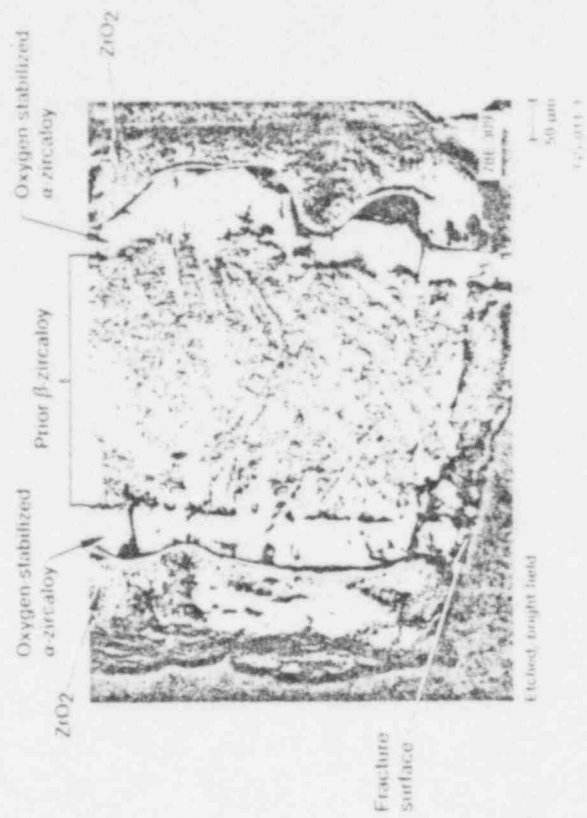
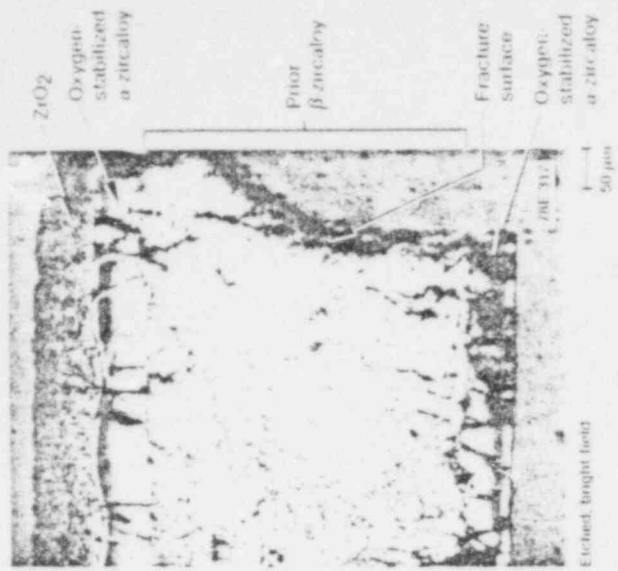


Fig. 8. Cross-sections of break-in cladding sections.

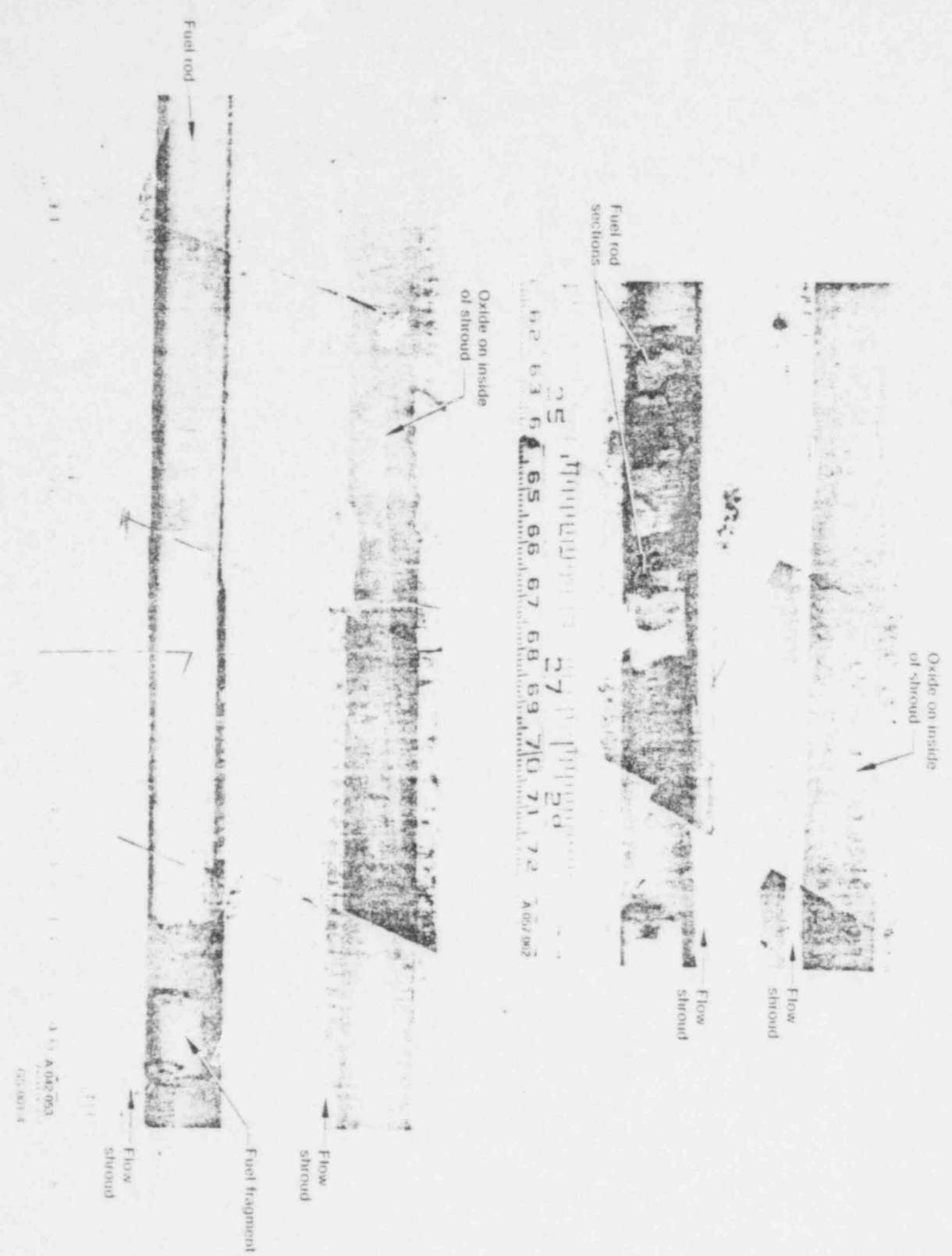


Fig. 9 Overall view of surface roughness in oxide on the inner surface of the shroud

### 3. FUEL FAILURE MECHANISMS AND BREAKUP

A large amount of the fuel disintegrated during testing. A total of 153 grams (24% of the  $\text{UO}_2$  fuel stack) broke up into pieces less than  $76 \mu\text{m}$  in diameter and was swept through the shroud screens by the coolant. The loose fuel remaining in the shroud and screens was sieved and weighed to give a particle size distribution. The details of this analysis are presented in Appendix D. However, sections of fuel greater than one pellet in length without cladding remained intact. From posttest evidence alone it is not clear at what time during the test the fuel broke up.

On-line measurements indicated most of the fuel fragmentation and loss occurred as a result of thermal shock upon cooling. The fission product detection system gave indications of gross rod failure at shutdown. Indications of flow blockage (up to 80%) were observed only at shutdown. Although the embrittled cladding failed during the test from a combination of stresses, including the pressure drop across the cladding and stresses induced by fuel thermal expansion against the cladding, a driving force for fuel fragmentation did not exist at that time. After the preconditioning operation to introduce fuel cracking, only limited fracturing is likely to have occurred during the film boiling operation. However, fuel fragmentation at grain boundaries due to thermal shock at shutdown is expected to have occurred (Subsection VI-3).

Test PCM-1 was operated with a significant fraction of the test rod fuel stack in the molten state to increase the probability of molten fuel interaction with the coolant. No fuel was found solidified on the outside surface of the intact portions of the rod, nor were pieces of solidified fuel found in the debris around the bottom or top end caps. Some small fuel particles were found in the screens located in the ends of the shroud; however, none of these pieces appeared to have been molten. If molten fuel was in contact with the coolant, the material was either dispersed on contact with the coolant or shattered after solidification into pieces small enough ( $<76 \mu\text{m}$ ) to pass through the shroud particle screens. The exposure of the fuel to a steam environment at approximately 520 seconds into the transient resulted in changes in the structure and properties of the fuel, including the existence of unusual porosity gradients. The presence of  $\text{U}_4\text{O}_9$  in the fuel following the test indicates a higher oxygen content than existed at the beginning of testing, which would result in lower fuel melting temperatures and accelerated grain growth. The changes in properties probably affected the breakup of the fuel. (The changes in the fuel are discussed in Section VI.)

## IV. FUEL ROD TEMPERATURE PROFILE

Post-DNB fuel rod cladding phase changes and oxygenation by zircaloy-coolant and  $UO_2$ -zircaloy reactions are processes that influence the cladding ductility. The principal variables controlling these processes are time in film boiling and cladding temperature. The cladding ductility greatly influences cladding deformation and fuel rod failure. Knowledge of the axial and circumferential temperature gradients along the region of film boiling is required to understand fuel rod thermal and mechanical behavior. The temperature distribution data are especially required for model evaluation.

In-pile measurements of temperatures from cladding thermocouples do not give an accurate indication of film boiling temperatures due to a large fin cooling effect from the thermocouples attached to the fuel rod (180 to 220 K reduction in temperature for Test PCM-1). The thermocouples do respond to changes at the beginning of the temperature transient and, therefore, provide good indications of the onset of film boiling, but postirradiation analysis is necessary to determine the cladding temperature during the transient. Two methods were used to determine cladding temperatures: (a) metallographic examination to correlate the cladding microstructures to temperatures associated with specific phase transformations in zircaloy, and (b) computation based on kinetic correlations that relate the sum of the external surface  $ZrO_2$  layer thickness and the adjacent oxygen-stabilized alpha layer measured metallographically with the duration of film boiling. From these examinations and calculations, axial and circumferential cladding surface temperature profiles were estimated. A radial temperature profile of the rod was also estimated at two elevations, using the fuel surface temperatures to confirm the estimated cladding temperatures.

### 1. AXIAL PROFILE

Posttest microstructures can be associated with the various phase changes that occur in zircaloy at specific phase transformation temperatures. Recrystallization of the as-fabricated, stress relieved zircaloy to equiaxed alpha-zircaloy occurs at about 920 K. A two-phase mixture of alpha- and beta-zircaloy exists in the temperature range from 1105 to 1245 K. Above 1245 K, beta zircaloy is the stable phase.

The cladding near the top of the film boiling zone was examined metallographically. Equiaxed alpha grains with a small amount of prior beta structure were found at the 0.82-m elevation, indicating that the temperature at this location was about 1150 K. The 0.79-m elevation exhibited a larger amount of beta in the equiaxed alpha structure but was still in the two-phase region and, therefore, at a maximum temperature of less than 1245 K. Previously molten cladding existed at the cladding center between two oxide layers at the 0.30-m elevation and in one of the loose pieces of rod located between 0.37 and 0.58 m. Melting of the cladding may have occurred over as much as 31% of the fuel rod. Most of the cladding in this region was missing posttest. The melting indicates a cladding temperature of at least 2100 K.

Isothermal effective temperatures were calculated using measured outer surface oxide layer, oxygen-stabilized alpha layer, and  $\xi$  layer (combined oxide plus alpha) thicknesses. The isothermal effective temperature is defined as the temperature at which cladding oxidation equivalent to that measured metallographically would occur for the time in film boiling. The calculations were based on the isothermal kinetic correlations developed by Cathcart<sup>7</sup>. These correlations are as follows:

- (1) For the surface layer of  $ZrO_2$

$$X/t^{1/2} = 1500.67 \left( \begin{array}{c} +15\% \\ -12\% \end{array} \right) \exp \left[ - \frac{9031 \left( \pm 2.2\% \right)}{T} \right]$$

- (2) For the cladding (outer diameter) layer of oxygen-stabilized alpha

$$X/t^{1/2} = 12\,340.99 \left( \begin{array}{c} +27\% \\ -17\% \end{array} \right) \exp \left[ - \frac{1211 \left( \pm 2.6\% \right)}{T} \right]$$

(3) For the combined layer of  $ZrO_2$  and oxygen-stabilized alpha

$$\chi/t^{1/2} = 8260.75 \left( \begin{array}{c} + 8\% \\ - 7\% \end{array} \right) \exp \left[ - \frac{10493 \left( \begin{array}{c} +1.2\% \end{array} \right)}{T} \right]$$

where  $\chi$  is the layer thickness in  $\mu\text{m}$ ,  $t$  is the film boiling time in seconds, and  $T$  is the isothermal effective cladding temperature in K. Bracketed quantities refer to individual 90% confidence limits on the preexponential and activation energy terms.

The time at temperature for each axial location along the fuel rod was adjusted to reflect the progression of film boiling as indicated from the thermocouple response data obtained during the initiation of the transient. The axial position of film boiling is plotted in Figure 10 as a function of time in film boiling. The heavy, dark arrows correspond to actual thermocouple response times during film boiling operation. The dashed line indicates the estimated progression of film boiling to lower axial positions along the rod. The upper and lower film boiling boundaries probably shifted somewhat due to the power increase at 283 seconds; however, only the final film boiling boundaries are known.

The results of the isothermal cladding temperature estimate calculations using the film boiling times from Figure 10 for the 0.67- and 0.74-m elevations are presented in Table IV. These calculations were performed every 30 degrees circumferentially at these two elevations. The  $\xi$  layer thickness gives the most

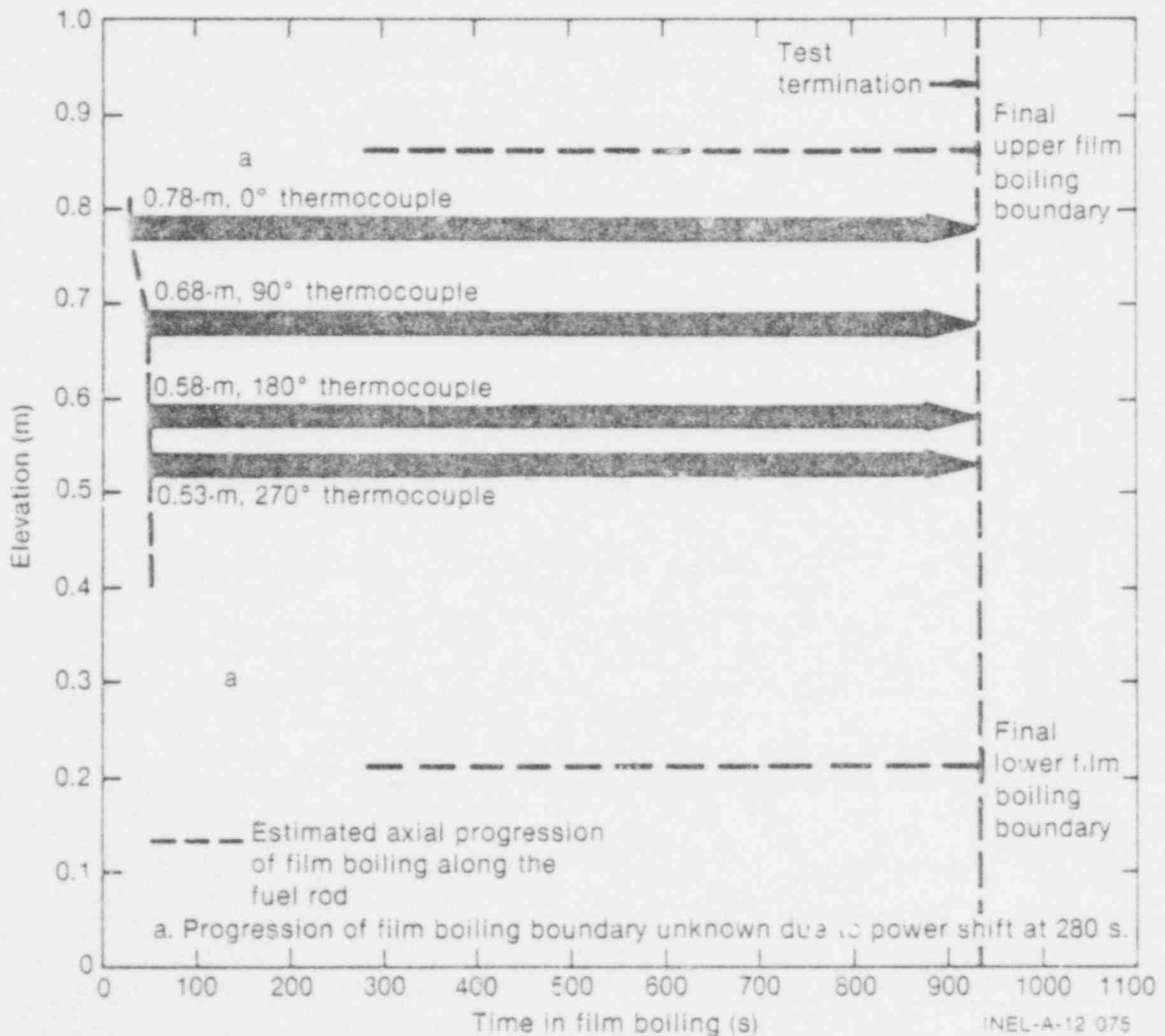


Fig. 10 Axial progression of film boiling from thermocouple response data.

TABLE IV

## CALCULATED EFFECTIVE ISOTHERMAL TEMPERATURES

Elevation from Bottom of Fuel Stack (m)	Orientation (°)	Outer Diameter ZrO <sub>2</sub> Layer		Outer Diameter α-Zircaloy Layer		ZrO <sub>2</sub> + α-Zircaloy		Total Cladding Wall Thickness (μm)	Effective Isothermal Temperature (±50 K)
		(μm)	T(K)	(μm)	T(K)	(μm)	T(K)		
0.67  Film boiling time t = 885 s	0	48	1321	288	1694	336	1591	624 <sup>a</sup>	1690
	30	136	1559	278	1686	414	1643	692	1640
	60	136	1559	178	1587	314	1575	690	1580
	90	120	1526	158	1563	278	1547	692	1550
	120	116	1517	134	1530	250	1523	686	1520
	150	103	1487	108	1490	211	1486	669	1490
	180	102	1485	93	1463	195	1470	700	1470
	210	100	1480	114	1500	214	1489	670	1490
	240	--	--	114	1500	114	1367	581 <sup>b</sup>	1500
	270	24	1260	110	1493	134	1396	612 <sup>b</sup>	1490
	300	40	1287	211	1623	251	1524	606 <sup>b</sup>	1620
	330	50	1329	237	1649	287	1554	628 <sup>b</sup>	1650
	360	53	1341	246	1657	299	1563	633	1660
0.74  Film boiling time t = 895 s	0	37	1272	42	1224	79	1304	654	1300
	30	40	1286	45	1344	85	1516	643	1320
	60	38	1277	42	1334	80	1306	633	1300
	90	30	1235	33	1299	63	1268	636	1270
	120	26	1212	46	1347	72	1289	654	1290
	150	21	1178	42	1334	63	1268	647	1270
	180	38	1277	29	1282	67	1278	628	1280
	210	34	1257	31	1291	65	1273	634	1270
	240	21	1178	25	1262	46	1222	621	1220
	270	13	1108	12	1172	25	1141	625	1140
	300	18	1155	24	1256	42	1209	646	1210
	330	30	1235	36	1312	66	1275	648	1280

a. Possible oxide spalling.

b. Oxide spalling.



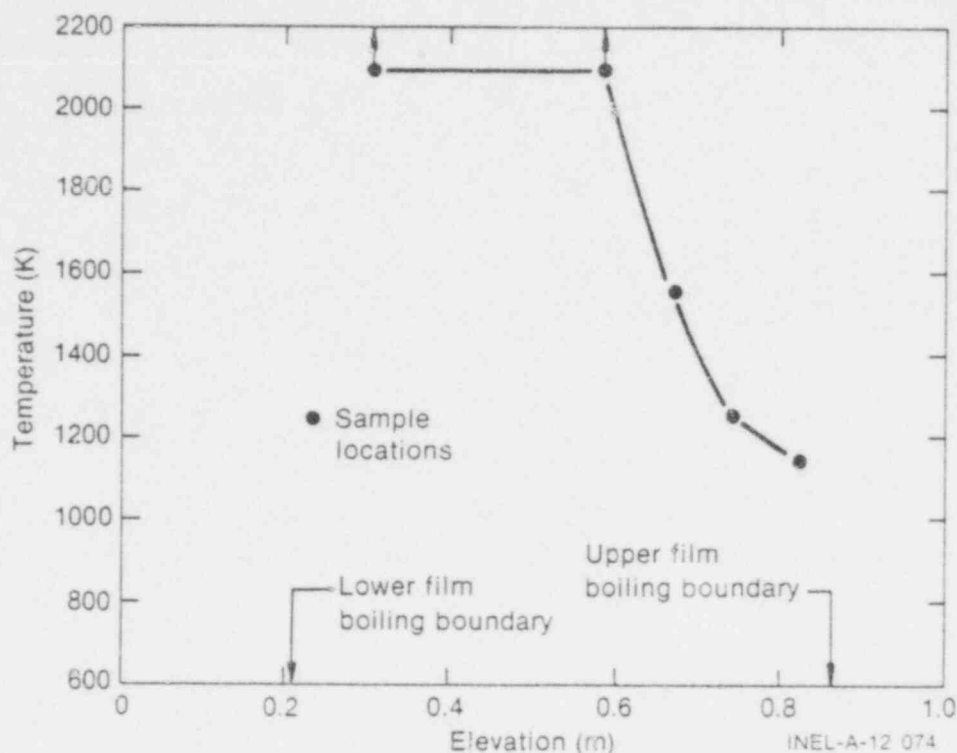


Fig. 11 Cladding temperature at several elevations as determined from microstructure and calculated from oxide thickness.

accurate temperature indication. However, at some locations the oxide layer had spalled off, giving incorrect  $\xi$  and oxide layer thicknesses. Therefore, at spalled locations the oxygen-stabilized alpha layer gave the more accurate temperature indication. The isothermal cladding temperature at 0.67 m ranged from 1470 to 1690 K with an average of 1565 K, and at 0.74 m ranged from 1140 to 1320 K with an average of 1260 K. The average cladding temperature calculated from oxide thicknesses at the 0.67- and 0.74-m elevations, plus those temperatures as determined from observed microstructure at the 0.30- and 0.82-m elevations are plotted in Figure 11.

## 2. CIRCUMFERENTIAL PROFILE

The calculated isothermal effective cladding temperatures at 0.67 and 0.74 m are plotted every 30 degrees azimuthally in Figure 12. Photomicrographs showing the change in cladding structures with the temperature gradient for the 0.67-m elevation are shown in Figure 13. Circumferential variation in rod power and, subsequently, fuel and cladding temperatures were not expected due to the single-rod test configuration with the fuel rod centered in the in-pile tube. However, there was a significant circumferential temperature gradient in the cladding, the maximum temperature being at 0 to 30 degrees and the minimum at 180 to 270 degrees for both elevations. A 220-K gradient existed at 0.67 m and a 180-K gradient existed at 0.74 m. A cladding thermocouple junction was located at the 90-degree orientation at 0.68 m. The minimum temperature was not at the thermocouple junction orientation. There was no thermocouple junction at 0.74 m. Therefore, the circumferential gradient was not a result of the cooling-fin effect from cladding thermocouple junctions. The 0.53- and 0.58-m thermocouples extended the length of the rod at 270 and 180 degrees, respectively. The thermocouple sheaths were not attached to the rod at either 0.67 or 0.74 m; however, there seemed to be a temperature lowering effect from the 270- and possibly the 180-degree thermocouple sheaths that were near the cladding but not attached.

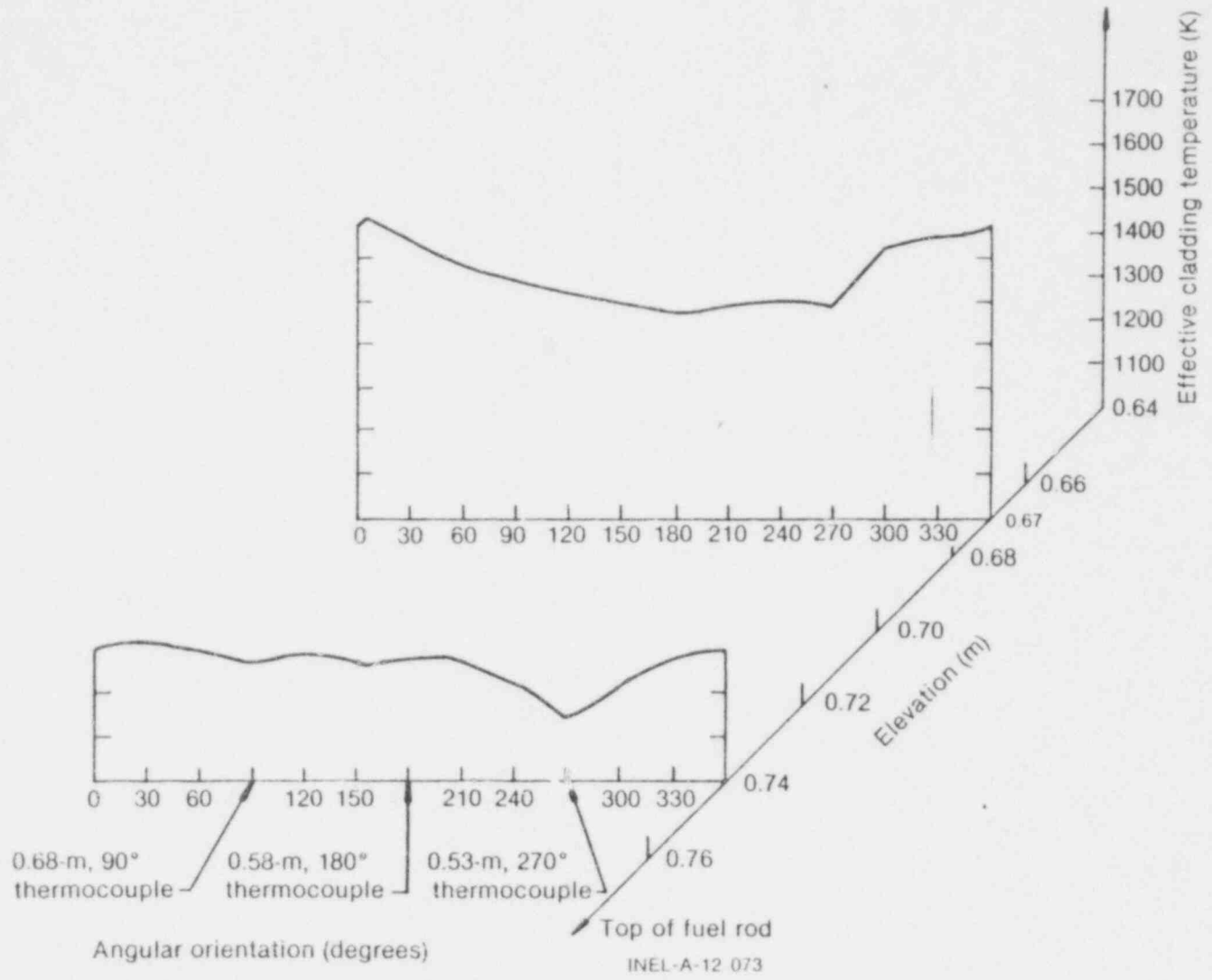


Fig. 12 Isometric plot of the isothermal effective cladding temperature as a function of angular orientation and axial position.

INEL-A-12 073

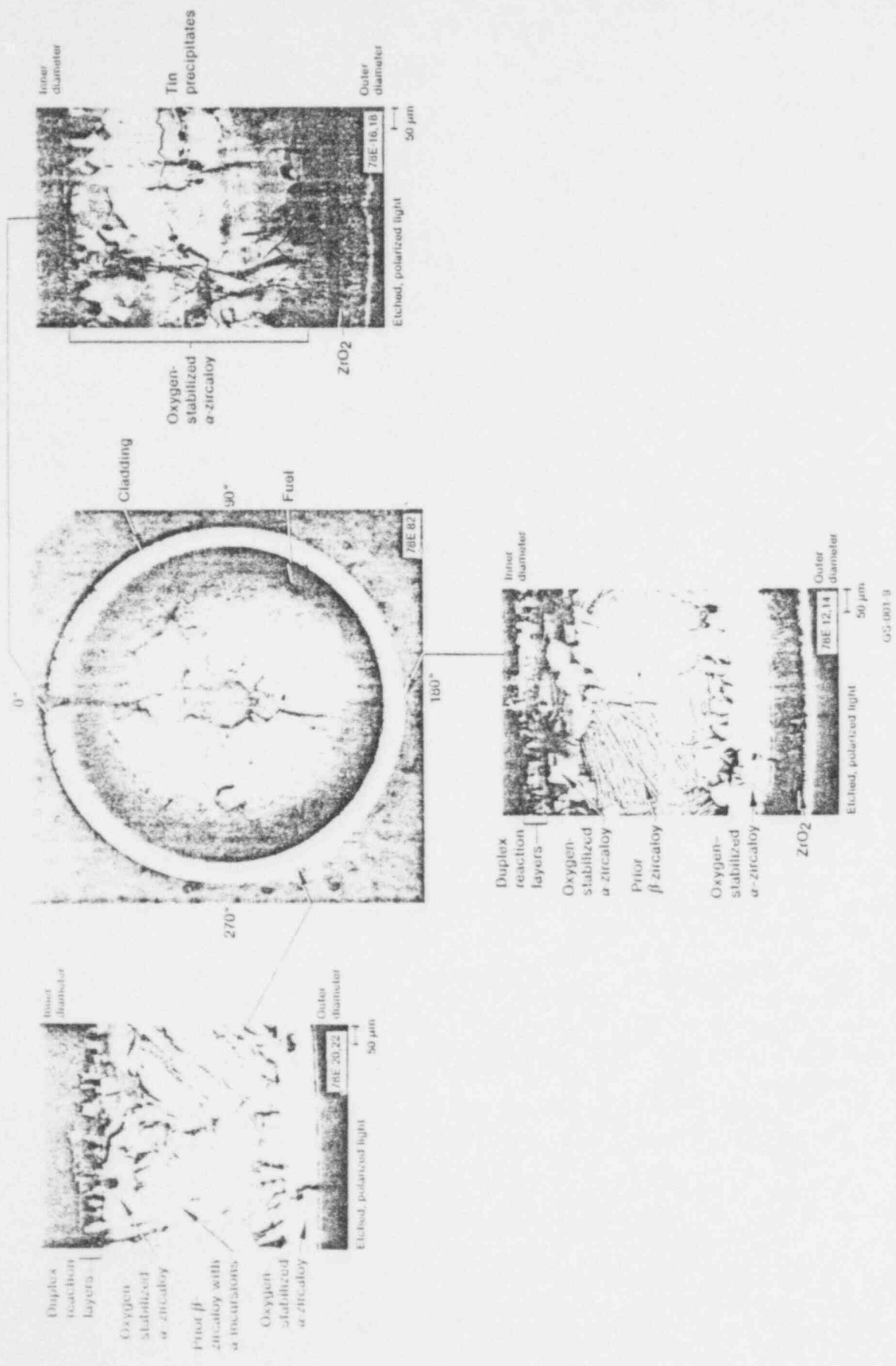


Fig. 13. Lading microstructure at 0.67 m, showing circumferential temperature gradient.

### 3. RADIAL PROFILE

Melt radii were determined at 15 cross sections in the Test PCM-1 fuel rod. Only three of these cross sections could be assigned definite elevations. The other twelve were the ends of six broken pieces of fuel rod lying in the middle third of the flow shroud and could only be assigned ranges of elevations. An approximate fuel surface temperature was calculated from the melt radius and local power was calculated through use of an equation of the form<sup>8</sup>

$$\frac{q}{4\pi} = \int k dT$$

where

q = local power

k = thermal conductivity of the fuel

T = temperature.

The pellet surface temperature could be used as an upper boundary for the cladding inside surface temperature. Table V presents the elevation, radial percent of melting, volume percent of melt, local power level, pellet surface temperature, and estimated cladding temperatures determined for each of the 15 cross sections.

Generally, the melt radii of the fuel rod fragments without cladding were smaller than those sections with cladding that were at equal or lower power locations. The implications of this observation on the fuel rod breakup scenario were discussed in Subsection III-3.

Simplified radial temperature profiles can be constructed for the 0.30- and 0.67-m elevations. The profiles are plotted in Figure 14. At 0.30 m, the temperature at the edge of the molten zone was approximately 3100 K. The temperature at the edge of the pellet, as calculated from the melt radius and local power, was 2350 K. The temperature drop across the ZrO<sub>2</sub> layer on the cladding inner surface was calculated to be 132 K assuming a thermal conductivity of ZrO<sub>2</sub> of 2.4 W/m·°C,<sup>9</sup> a power at this elevation of 73 kW/m, and a ZrO<sub>2</sub> layer thickness of 250 μm (metallographic observation). The temperature at the center of the cladding was about 2200 K, which correlates well with the metallographic indications that the center core of the cladding at this elevation was molten. The range of temperatures required to produce the microstructure observed is 2227 to 2273 K. (A discussion of the molten cladding microstructures is presented in Subsection V-2, on cladding-coolant reaction.)

Similarly, at the 0.67-m elevation, assuming a local power of 59 kW/m, the temperature at the edge of the pellet averaged 1750 K. (The molten fuel area appeared to be symmetrical within the pellet.) The cladding temperatures determined for this elevation from the reaction layer thicknesses ranged from 1470 to 1690 K. Thus, the calculation of pellet surface temperature is in reasonable agreement with cladding temperatures determined by metallography and oxide kinetics.

TABLE V  
FUEL MELT RADII DATA

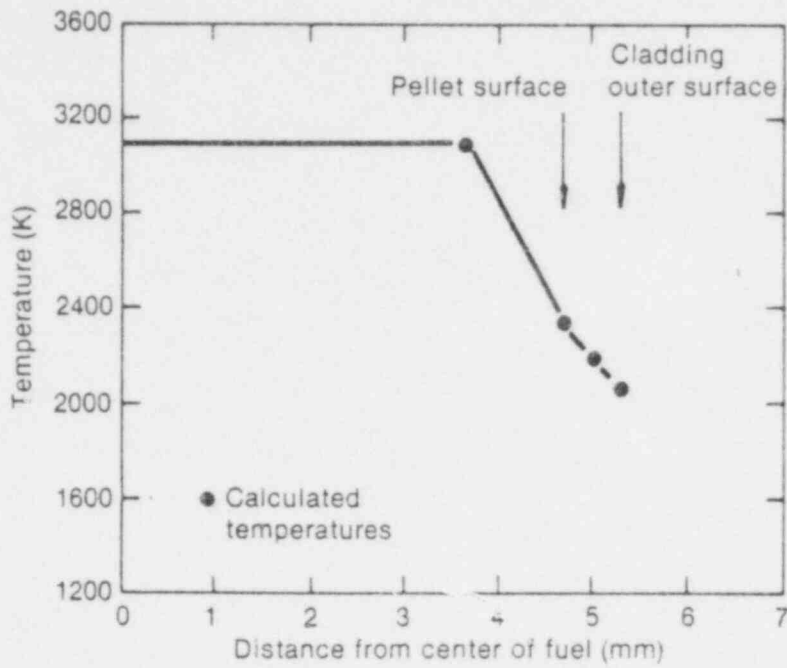
Actual Location (m)	Elevation Range (m)	Melt Radius (%)	Melt Volume (%)	Local Peak Power (kW/m)	Pellet Surface Temperature (K)	Estimated Cladding Temperature (K)
0.299	0.299	77	59	73	2350	2227 to 2273
0.310	0.299 to 0.507 (#6 bottom) <sup>a</sup>	56	31	73 to 78	1550 to 1700	b
0.327	0.316 to 0.524 (#6 top)	56	31	74 to 78	1550 to 1700	
0.433	0.316 to 0.524 (#5 bottom)	62	38	74 to 78	1500 to 1850	b
0.457	0.340 to 0.548 (#5 top)	65	42	73 to 78	1800 to 1900	
0.464	0.340 to 0.548 (#4 bottom)	67	45	73 to 78	1850 to 2000	b
0.480	0.356 to 0.564 (#4 top)	82	67	71 to 78	2300 to 2500	
0.503	0.356 to 0.564 (#3 bottom)	78	61	71 to 78	2200 to 2400	c
0.519	0.372 to 0.580 (#3 top)	82	67	70 to 78	2300 to 2500	
0.529	0.372 to 0.580 (#2 bottom)	82	67	70 to 78	2300 to 2500	c
0.542	0.385 to 0.593 (#2 top)	82	67	62 to 78	2300 to 2500	
0.588	0.385 to 0.593 (#1 bottom)	85	72	68 to 78	2400 to 2500	c
0.630	0.427 to 0.635 (#1 top)	83	69	62 to 77	2400 to 2500	
0.670	0.670	36	13	59	1750	1470 to 1690
0.743	0.743	0	0	50	--	1140 to 1320

a. Numbers refer to broken fuel rod sections as identified in Figure 6.

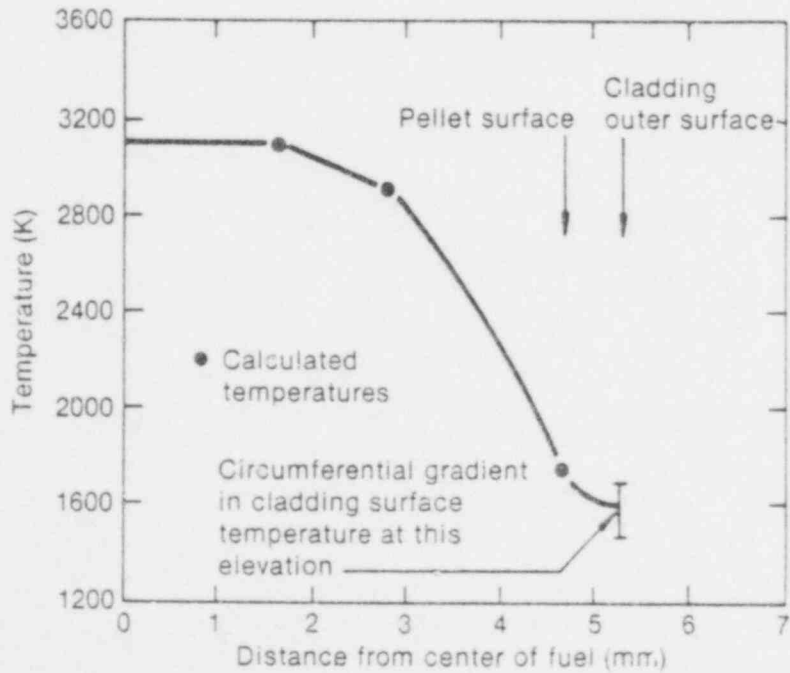
b. Fuel rod sections without cladding.

c. Cladding was all ZrO<sub>2</sub> posttest.

631-190



(a) 0.30-m elevation



(b) 0.67-m elevation INEL-A-12 080

Fig. 14 Fuel rod radial temperature profile at 0.30 and 0.67 m.

## V. CLADDING CHEMICAL REACTIONS

Considerable chemical interaction of the cladding with the steam environment and the fuel occurred in Test-PCM-1. In some locations the entire cladding wall was oxidized to  $ZrO_2$ . The following sections discuss the interaction of the cladding with the  $UO_2$  fuel and the steam blanket. After initial rod failure, a steam environment existed inside a portion of the fuel rod. The effect of the steam environment on the cladding oxidation is evaluated. The embrittlement of the cladding by oxidation and hydriding are discussed.

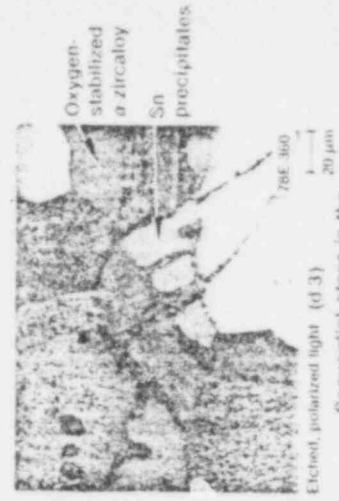
### 1. FUEL-CLADDING REACTION

It has been observed that, in general, oxygen diffuses from the  $UO_2$  into the beta-phase zircaloy, inducing an inner cladding surface layer transformation to oxygen-stabilized alpha-zircaloy. Frequently, when the fuel and cladding are in contact at high temperature, a duplex reaction layer will develop together with the oxygen-induced transformation of beta-phase material to oxygen-stabilized alpha-zircaloy. The duplex layer consists of a uranium-rich layer adjacent to the cladding and a zirconium-rich layer adjacent to the fuel<sup>9</sup>. No duplex reaction layer will form if  $ZrO_2$  is present on the cladding inner surface<sup>9,10</sup>.

Examples of the Test PCM-1 zircaloy cladding structure that was oxidized by steam from the outside and reacted with the  $UO_2$  fuel on the inside is shown in Figure 15. All of the photographs in Figure 15 are of cladding at the same elevation (0.67 m), but different orientations. A 220 K circumferential temperature gradient existed at this elevation. Microprobe examination of the fuel-cladding reaction layers showed that as the oxygen-stabilized alpha layers from the inside and outside of the cladding grew to meet in the center, the U-rich and Zr-rich reaction layers became dispersed within the inner alpha layer. (Details of the microprobe examination are presented in Appendix E.) The alloying element, tin, was rejected into the boundary between the alpha and beta phases ahead of the advancing oxygen-stabilized alpha-phase boundary. The tin was eventually collected as metallic inclusions at the midpoint of the cladding. Three sequential steps in the segregation process are also shown in Figure 15. The microstructures at 0.67 m and above are typical of an unfailed fuel rod with no exposure of the cladding inside surface to steam. The absence of steam exposure above 0.67 m was due to cladding collapse onto the fuel column which sealed the top portion of the rod above the fracture at 0.63 m and isolated the plenum from the failure location. The plenum pressure transducer did not respond to the rod failure until communication between the plenum and the remainder of the rod was reestablished at shutdown.

The typical duplex layers were difficult to distinguish in much of the Test PCM-1 cladding because of the extensive chemical interaction of the fuel, cladding, and coolant due to the length of time at high temperatures and the ingress of water in the lower portions of the rod after failure. The cladding at the 0.30 m elevation had an oxide layer on both the outer and inner surfaces, with a core of molten material. Extensive microprobe analysis of this cladding was conducted, the results of which are presented in Appendix E. An inner oxide layer, with uranium diffused through it, existed at all orientations. The diffused uranium was probably a remnant of the duplex reaction layer which had existed prior to the ingress of steam into the rod.

The distribution of uranium in the inner oxide layer at the 0.30-m elevation is shown in Figure 16 for several circumferential locations. Uranium was present throughout the inner oxide layer at 290 degrees (the fracture location). This layer was approximately 110  $\mu m$  thick. The uranium penetrated to between 45 and 55  $\mu m$  of the 210- $\mu m$ -thick oxide layer at 235 degrees. The uranium penetration appeared to terminate at a separation in the inner surface oxide, which probably marked the duplex reaction layer penetration. At 210 degrees, uranium was found as far as 140  $\mu m$  into the 340- $\mu m$ -thick oxide layer. This penetration is approximately 40% of the total inside surface oxide layer. The concentration of uranium was highest in the 40  $\mu m$  of the inner surface oxide near the center of the cladding wall. Microprobe examination showed a definite layer formation in the inner surface oxide at 165 and 125 degrees. At 165 degrees, the layers in the oxide appeared to correspond to the duplex reaction layers observed during previous PCM examinations. The higher uranium level was between 160 and 80  $\mu m$ , and the lower level was between 80  $\mu m$  and the



Sequential steps in the Sn segregation process

GS-911-A

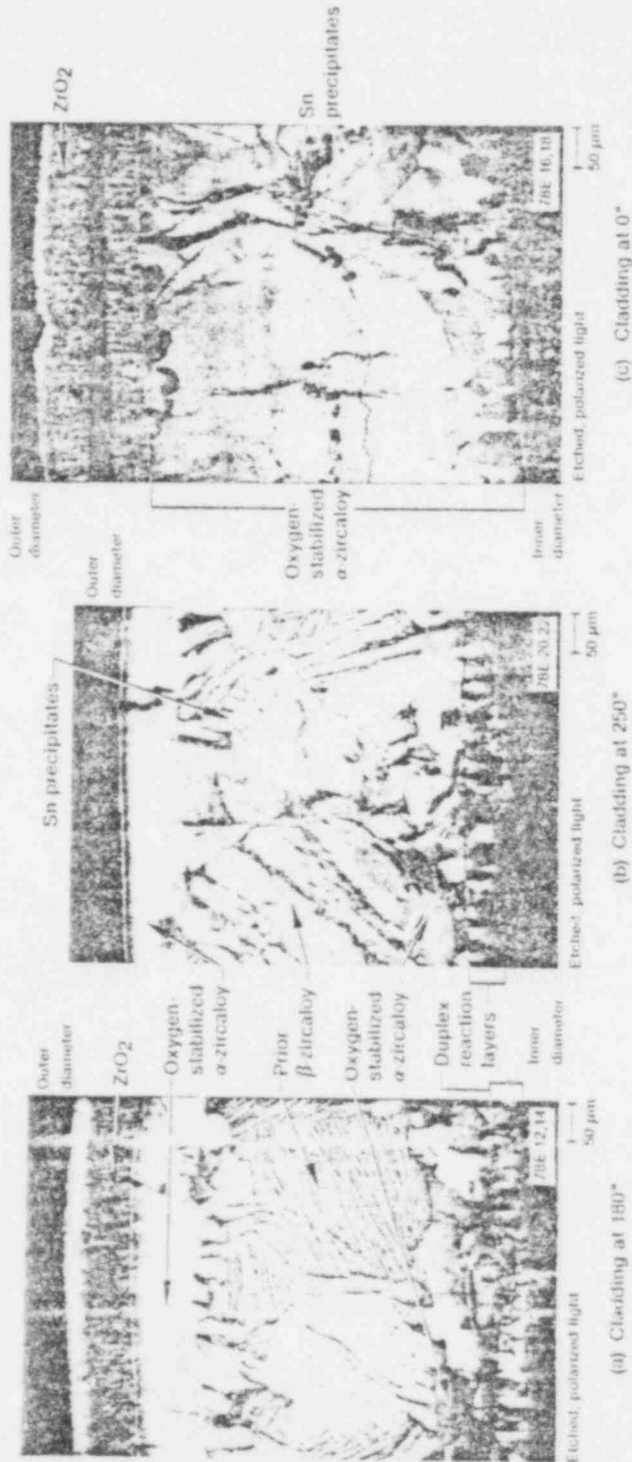


Fig. 15. Several orientations of the cladding at 0.67 in showing typical  $\alpha$  zircaloy  $\text{VO}_2$  zircaloy strain interactions.

631 193



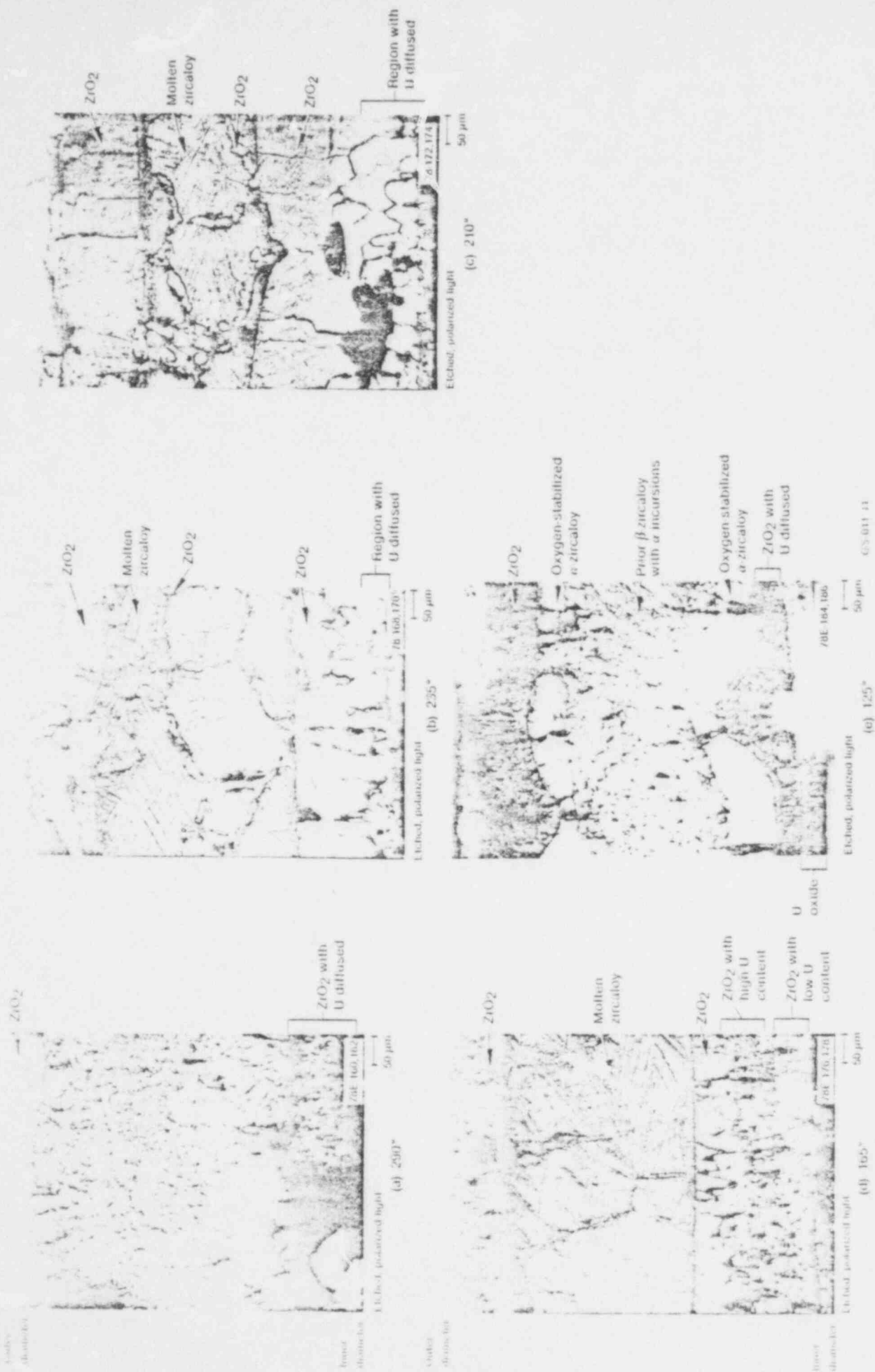


Fig. 16. Uranium distribution in the inner oxide layer at several orientations of the  $\theta$  in elevation.

inner surface. The zirconium content was constant across this region. Normally, the duplex reaction layers consist of a zirconium-rich layer near the fuel, followed by a uranium-rich layer. The 125-degree location in Figure 16 had four layers in the inner diameter oxide. Uranium was found in all of the oxide layers except for the layer closest to the alpha-zircaloy. The two layers closest to the fuel contained uranium and no zirconium (Figure 16). There was no visible difference in the oxide containing uranium and zirconium, and the oxide containing only uranium. The uranium distribution in the inner oxide layer at all orientations suggests the minimum depth of the oxygen-stabilized alpha penetration, including the duplex reaction layers existing before exposure of the inside surface to steam from the rod failure. The penetration ranged from 45 to 160  $\mu\text{m}$  into the cladding.

The two pieces of broken fuel rod with cladding intact (located at 0.52 and 0.59 m) were examined. The cladding had completely oxidized at these two locations. Diffusion bonding between the fuel and cladding existed at all locations investigated on these two rod fragments; however, the penetration of uranium into the oxidized cladding varied from nil to 80  $\mu\text{m}$ . Interaction regions at 0.59 m containing uranium in the cladding are shown in Figure 17. In this figure it can be seen that the interaction region at 0.59 m varied from 0 to 50 to 80  $\mu\text{m}$  for the 0-, 180-, and 90-degree orientations, respectively. Uranium penetration into the cladding only occurred at locations where molten fuel was in contact with the cladding at 0.52 m. The absence of uranium dispersed in the oxidized cladding, shown in Figure 17, indicated that the cladding melted early in the transient so that the fuel-cladding interaction was between  $\text{UO}_2$  and molten zircaloy. The products of such an interaction are  $\text{ZrO}_2$  and metallic uranium<sup>12</sup>. The uranium apparently does not penetrate the newly formed  $\text{ZrO}_2$  layer. The formation of  $\text{ZrO}_2$  from both the inner and outer cladding surfaces continues until the molten cladding is totally transformed to solid oxide.

Molten fuel made contact with the cladding at two orientations at 0.52 m, with significant mixing of the cladding and fuel materials occurring. At 335 degrees, uranium was present halfway through the cladding and zirconium penetrated the fuel as far as the large, nearly pore free grains that define, at other locations, the maximum fuel melt radius. Only small amounts of zirconium were present in the molten fuel near the pellet surface at the 135-degree orientation. The cladding apparently broke away at this orientation before more extensive mixing could occur.

## 2. CLADDING-COOLANT REACTION

In general, the oxidizing reaction from the zircaloy-water (steam) interaction produces oxygen concentration gradients ahead of the advancing oxide layer. The oxygen uptake in beta-zircaloy induces transformation of the beta-phase material to oxygen-stabilized alpha-phase. The zircaloy microstructures generally observed metallographically at ambient temperatures are thus composed of distinct phases of surface oxide, oxygen-stabilized alpha, and the prior beta-phase field matrix. When zircaloy is exposed to steam for extended periods of time, as in Test PCM-1 (15 minutes), the zircaloy can become completely oxidized to  $\text{ZrO}_2$ . The oxidation kinetic relations which fit semi-infinite diffusion conditions no longer strictly hold when the beta-phase thickness becomes small compared with the  $\text{ZrO}_2$  and oxygen-stabilized alpha thicknesses. In addition, the increasing oxidation of the cladding insulates the fuel pellet, subsequently raising the fuel temperature and, therefore, the cladding temperature. The oxidation rate increases with the increasing temperature.

Some oxide spalling occurred at locations where the cladding was completely oxidized to  $\text{ZrO}_2$ . The volume ratio of  $\text{ZrO}_2$  to zircaloy is 1.54. The original wall thickness of the cladding was 620  $\mu\text{m}$ . The wall thickness after complete oxidation should be 955  $\mu\text{m}$ . The two elevations examined, at which the cladding wall thickness was totally oxidized to  $\text{ZrO}_2$ , were at 0.59 and 0.52 m. The wall thickness measured at several orientations of these samples (loose pieces of fuel rod with cladding) ranged from 880 to 900  $\mu\text{m}$  at 0.59 m and from 765 to 900  $\mu\text{m}$  at 0.52 m. A maximum of 8% of the oxide spalled away at 0.59 m and 20% at 0.52 m; thus, the totally oxidized cladding remained nearly intact at these locations.

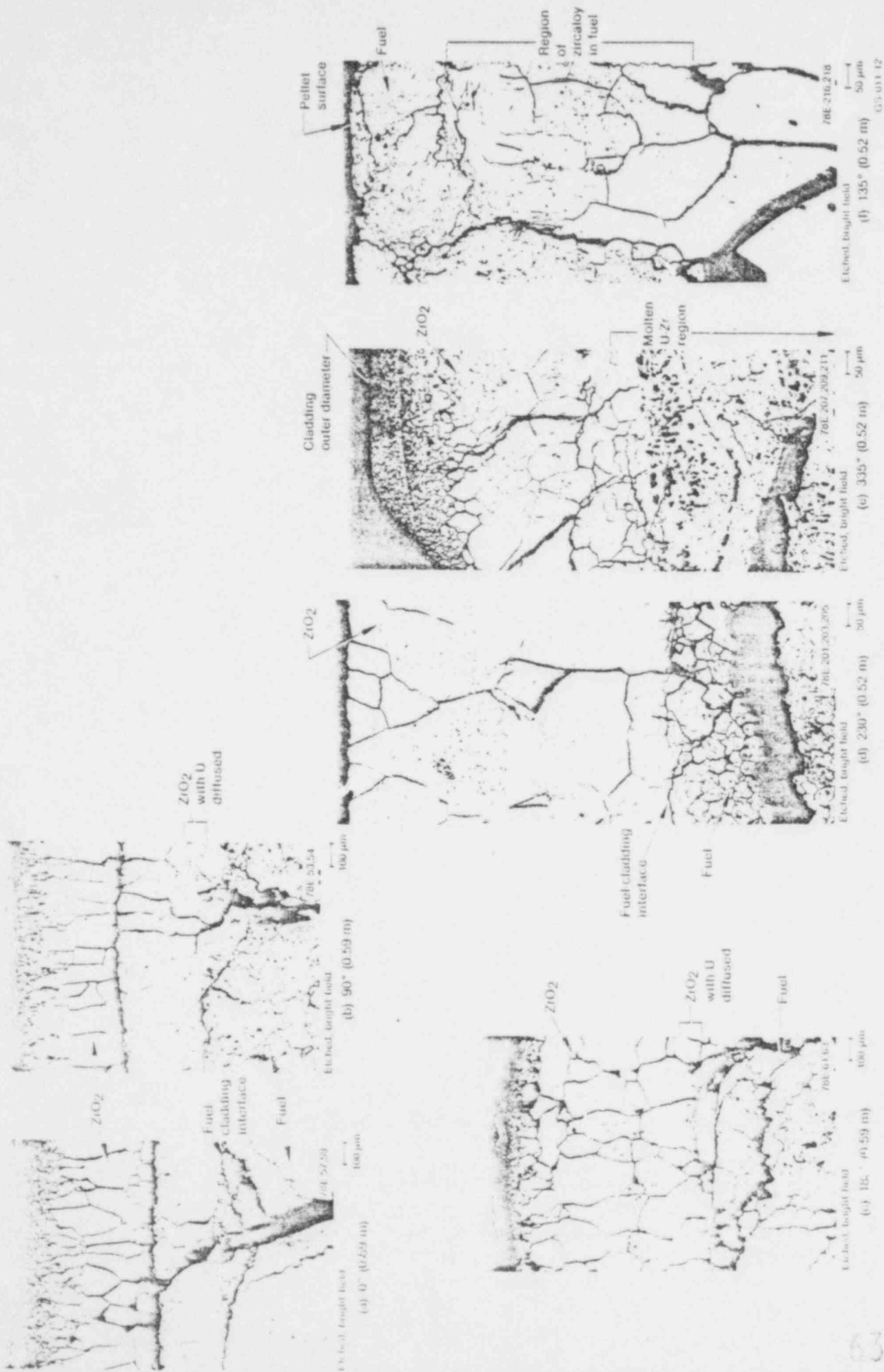


Fig. 17. Uranium distribution in the oxidized cladding at 0.59 and 0.52 m.

Once the zircaloy cladding completely oxidizes to  $ZrO_2$ , it, like the  $UO_2$  fuel, is a ceramic. Some examples of the oxidized cladding are shown in Figure 18. In all of the locations shown, grain growth and porosity were observed in the oxidized cladding. Layering of the outer surface of the totally oxidized cladding was not as apparent as in oxide layers on metallic zircaloy cladding at other locations of the rod.

The cladding melting observed at the 0.30-m elevation is a complicated process that can be somewhat explained by the microstructure of the cladding (Figure 19) with reference to the zirconium-oxygen phase diagram (Figure 20). Three different orientations are shown in Figure 19, with progressively greater extents of oxidation. The microstructure suggests one phase (not oxygen-stabilized alpha) in equilibrium with  $ZrO_2$  in the form of layers on the outer and inner surface of the cladding and along what appear to be prior beta grain boundaries at temperature. (Microprobe examination identified the material to be  $ZrO_2$ .) The phase diagram shows that the other phase must be liquid zircaloy.

Proceeding from the outside to the inside surface, initially there probably existed layers of  $ZrO_2$ , oxygen-stabilized alpha, prior beta zircaloy, oxygen-stabilized alpha, and probably U-Zr interaction layers. It is postulated that after the layers had formed, the inside surface was exposed to a steam environment. An oxide layer formed on the inside surface, consuming the U-Zr interaction layers. The continued oxidation of the external cladding surface served to insulate the fuel rod, causing fuel and cladding temperatures to increase. The temperature of the cladding reached an elevated value such that the beta grains melted and the oxygen-stabilized alpha and  $ZrO_2$  did not. As more oxygen was added to the system, the oxygen-stabilized alpha was transformed to  $ZrO_2$ . The material was then cooled. There is an area of unusual morphology on either side of the molten zone, as seen in Figure 19, that may represent the oxygen-stabilized alpha zone at the onset of cladding melting. The dendritic platelets in the center region of the cladding wall that formed upon solidification of the melt are also shown in Figure 19.

The zirconium-oxygen phase diagram (Figure 20) shows the alpha plus liquid range to be between 2227 and 2273 K at less than 20 at. % oxygen. At these temperatures the beta phase melts. The alpha phase then transforms to  $ZrO_2$  with the addition of oxygen; however, the beta phase remains molten. After all of the alpha was transformed to  $ZrO_2$ , the temperature may have risen some, but not above the  $ZrO_2$  liquidus line.

### 3. CLADDING EMBRITTLEMENT

The mechanical behavior of the cladding is modified by the oxidation as well as the phase transformation processes that occur. The beta phase in the zircaloy has lower oxygen solubility than the oxygen-stabilized alpha phase and remains somewhat ductile through and following a film boiling transient. Several embrittlement criteria have been developed, usually based on the remaining beta phase.

The 17% ECR (equivalent cladding reacted to  $ZrO_2$ ) embrittlement criterion is currently used for reactor licensing. The ECR is a calculation of the total oxygen content in the product reaction layers and in the beta phase used to determine the fraction of the zircaloy capable of being oxidized to  $ZrO_2$ . The relationship between ECR and the product reaction layers is of the form<sup>13</sup>

$$\%ECR = \left( \frac{100}{t_w} \right) \left[ \frac{\text{Oxide Thickness}}{1.54} + \frac{\text{Alpha Thickness}}{1.54\alpha} \right]$$

where  $t_w$  is the cladding wall thickness, 1.54 is the oxide-to-metal volume ratio for  $ZrO_2$ -Zr, and  $\alpha$  is the ratio of the weight fraction of oxygen in  $ZrO_2$  to the average weight fraction of oxygen in the oxygen-stabilized alpha phase. This equation assumes that the total oxygen uptake is approximately equal to the oxygen contained in the surface oxide layers and the two-sided alpha product layers. The oxygen content in the beta phase has been assumed to be negligible.

The 17% ECR criterion indicates embrittlement of the cladding when the cladding is subjected to thermal quenching stresses generated by rewetting<sup>14</sup>; however, for operation at cladding temperatures of 1800 to 1850 K (the average cladding temperature during film boiling determined from the maximum thermocouple measurements and FRAP analysis for Test PCM-1)<sup>3</sup>, embrittlement would only be expected when

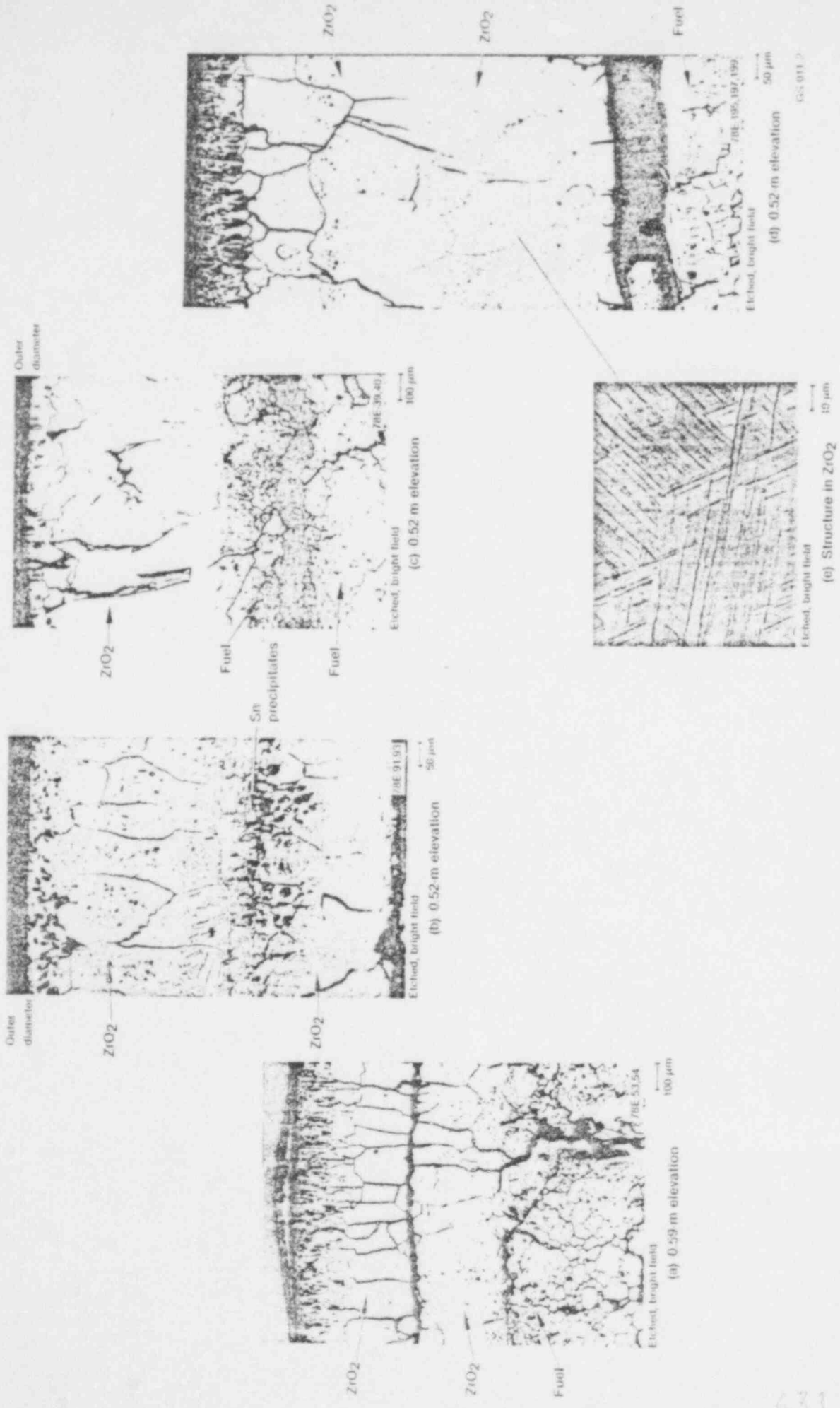


Fig. 18 Example of totally oxidized cladding.

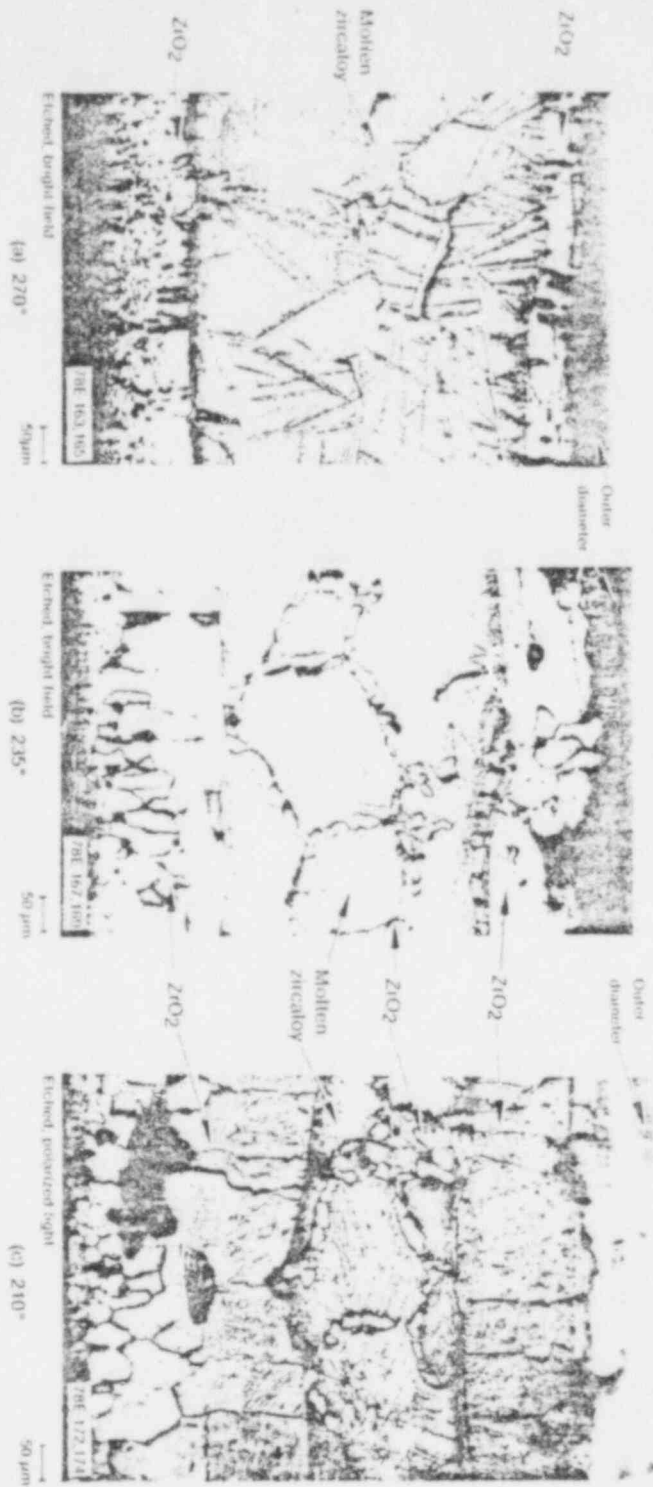
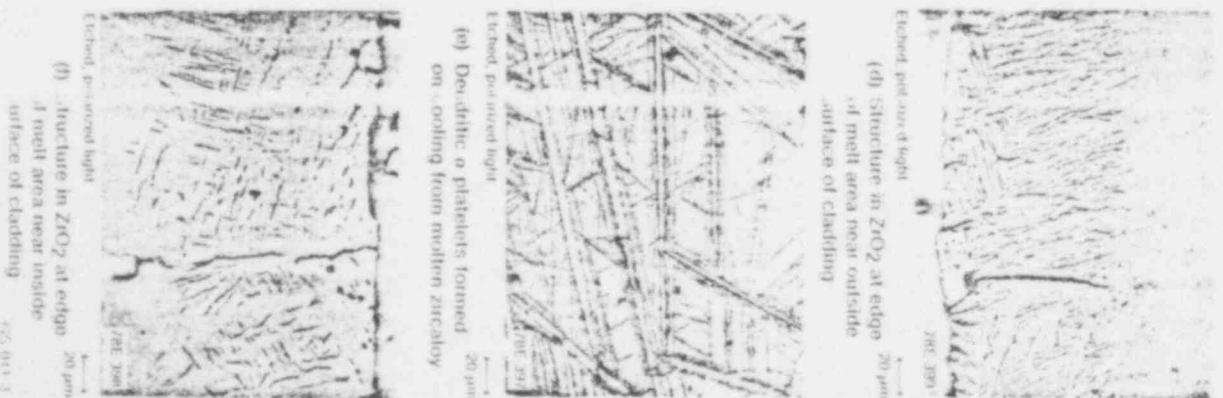


Fig. 19 Etching at 0.30 m showing progressively greater extent of oxidation and less etching.



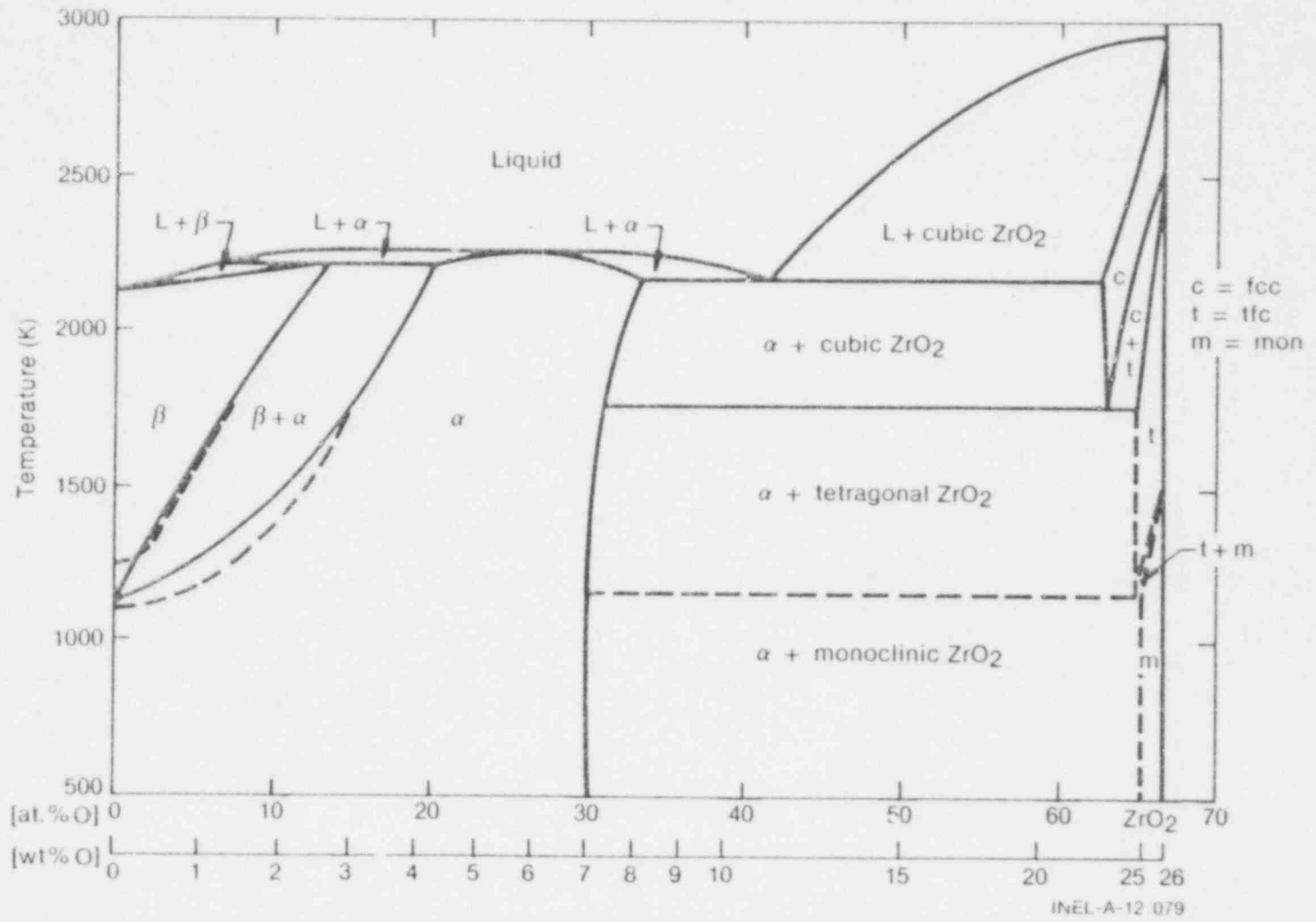


Fig. 20 Zirconium-oxygen equilibrium phase diagram.

631 200

the beta phase is entirely consumed (24% ECR). This estimated criterion for high temperature embrittlement is based on extrapolation of  $F_w$  (fractional wall thickness of remaining beta phase) and nil-ductility temperature published by D. O. Hobson<sup>15</sup>. Between 1800 to 1850 K, 24% ECR is reached after 515 to 580 seconds. Instrumentation gave indication of rod failure at approximately 520 seconds. It is reasonable to assume that the initial rod failure occurred as a result of cladding embrittlement.

After posttest examination, the cladding was brittle at ambient temperatures, at least between 0.30 and 0.67 m. However, in this region there were sections of fuel rod with completely embrittled cladding (all  $ZrO_2$  or  $ZrO_2$  and oxygen-stabilized alpha) that remained intact. The local strains during quenching were apparently insufficient to fracture the cladding at some locations. Several examples of the various cladding structures are shown in Figures 21 and 22. Microhardnesses of the structures are given. The values given are usually the maximum and minimum of several readings.

The microhardnesses of these highly oxidized structures can be compared with the microhardness of typical zircaloy structure to obtain an indication of mechanical properties. Generally, the nominal room temperature hardness of as-received, stress relieved zircaloy has been measured over a range of hardnesses near 262 DPH, and as the cold-work begins to anneal out close to the recrystallization temperature at 920 K (the transformation from stress relieved to mixed, irregular shaped alpha grains or preequiaxed alpha structure), the nominal hardness decreases to around 227 DPH. Full recrystallization ( $920 < T < 1105$  K) to an equiaxed alpha-phase structure, with no observable grain growth, produces an additional drop in the hardness to 191 DPH. The hardness values begin to increase again, as the alpha plus beta two-phase structure develops ( $1105 < T < 1245$  K), to values equivalent to or greater than 278 DPH. Upon transformation to the beta phase (zircaloy temperatures  $T > 1245$  K), the nominal room temperature hardness of the matrix increases to the range 312 to 350 DPH or more, depending on the oxygen content. The highest hardness values measured were associated with the outer cladding surface layer of oxygen-stabilized alpha, with values ranging from 750 to 800 DPH. Alpha-phase incursions extending into the parent beta-phase field ranged from 375 to 425 DPH in hardness, and the inner cladding surface layer of oxygen-stabilized alpha measured from 330 to 800 DPH nominal hardness<sup>10,16</sup>.

Microhardnesses of the oxide layers in fuel rods tested in the PBF have not been previously reported. The previously molten Test PCM-1 zircaloy had a hardness of 514 to 607 DPH, which is comparable to the inner alpha layer microhardnesses observed in past PCM tests. The hardness of the Test PCM-1 outer layer of oxygen-stabilized alpha was 475 to 663 DPH, somewhat lower than typically observed. The inner layer was 514 to 663 DPH at locations with well-defined Zr- $UO_2$  reaction layers, and 708 to 803 DPH at locations with the reaction layers dispersed into the alpha layer. The hardness of the alpha plus beta two-phase region near the top of the film boiling zone was 190 to 295 DPH. The microhardness in the inner oxygen-stabilized alpha layers and the alpha plus beta two-phase region were comparable to those previously observed. The prior beta phase varied from 262 to 514 DPH in regions with well-defined reaction layers, to 557 to 607 DPH in regions with dispersed reaction layers. The higher microhardnesses observed in the prior beta phase were most likely due to the high oxygen content in this phase associated with the extensive oxidation of the cladding in this test. The microhardnesses in the fully oxidized regions of the Test PCM-1 cladding ranged from 440 to 800 DPH. None of the inner or outer surface oxide layers had a hardness over 800 DPH.

#### 4. CLADDING HYDRIDING

Hydrogen absorption from metal-water reaction modifies the microstructure of oxidized zircaloy cladding and reduces the ductility of zircaloy at low temperatures ( $< 570$  K), causing fractures during posttest handling. Hydrides precipitate in zircaloy when the terminal solid solubility of hydrogen is exceeded. The solubility of hydrogen in zircaloy may be from a few tens of parts per million to several hundred parts per million at the operating test temperature ( $\sim 1000$  K).

The only location at which hydridding of the cladding was observed in the Test PCM-1 fuel rod was near the top of the film boiling zone. Photographs at three elevations are shown in Figure 23. Hydridding was not observed at the other elevations examined, probably because of the extensive oxidation. Hydrogen



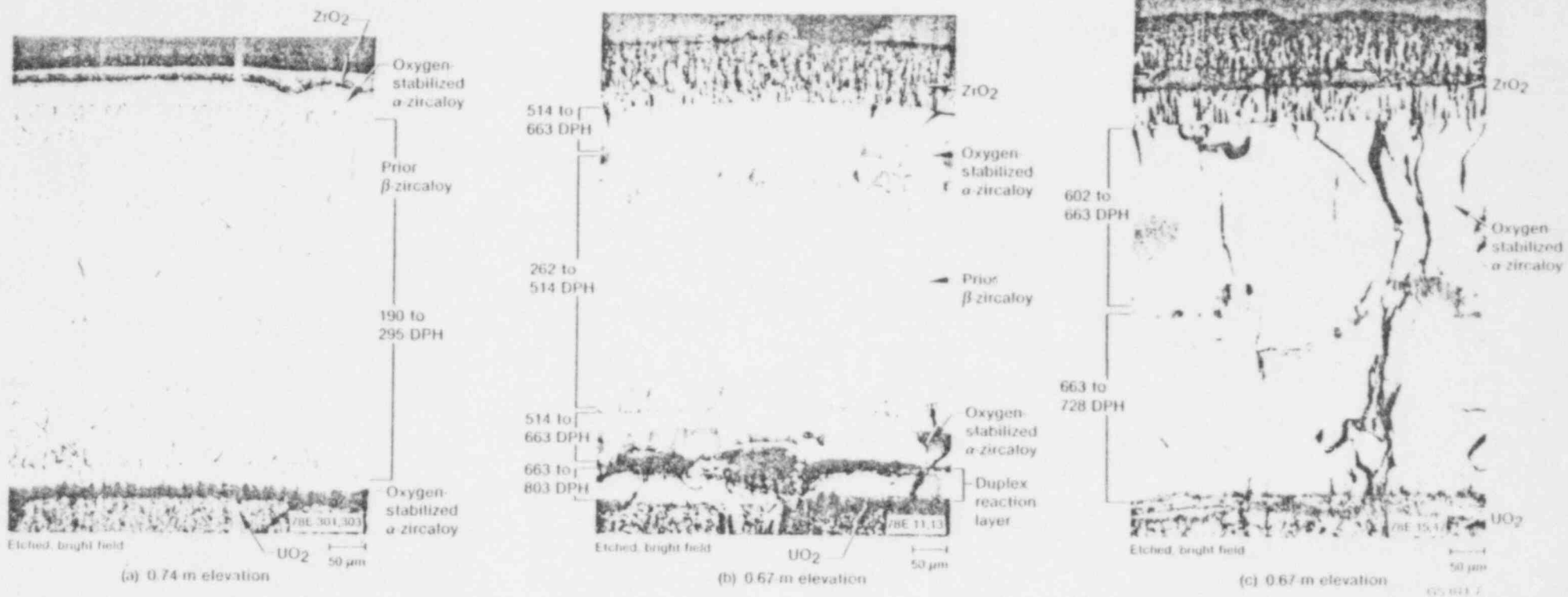


Fig. 21 Cladding microhardnesses at 0.67 and 0.74 m.

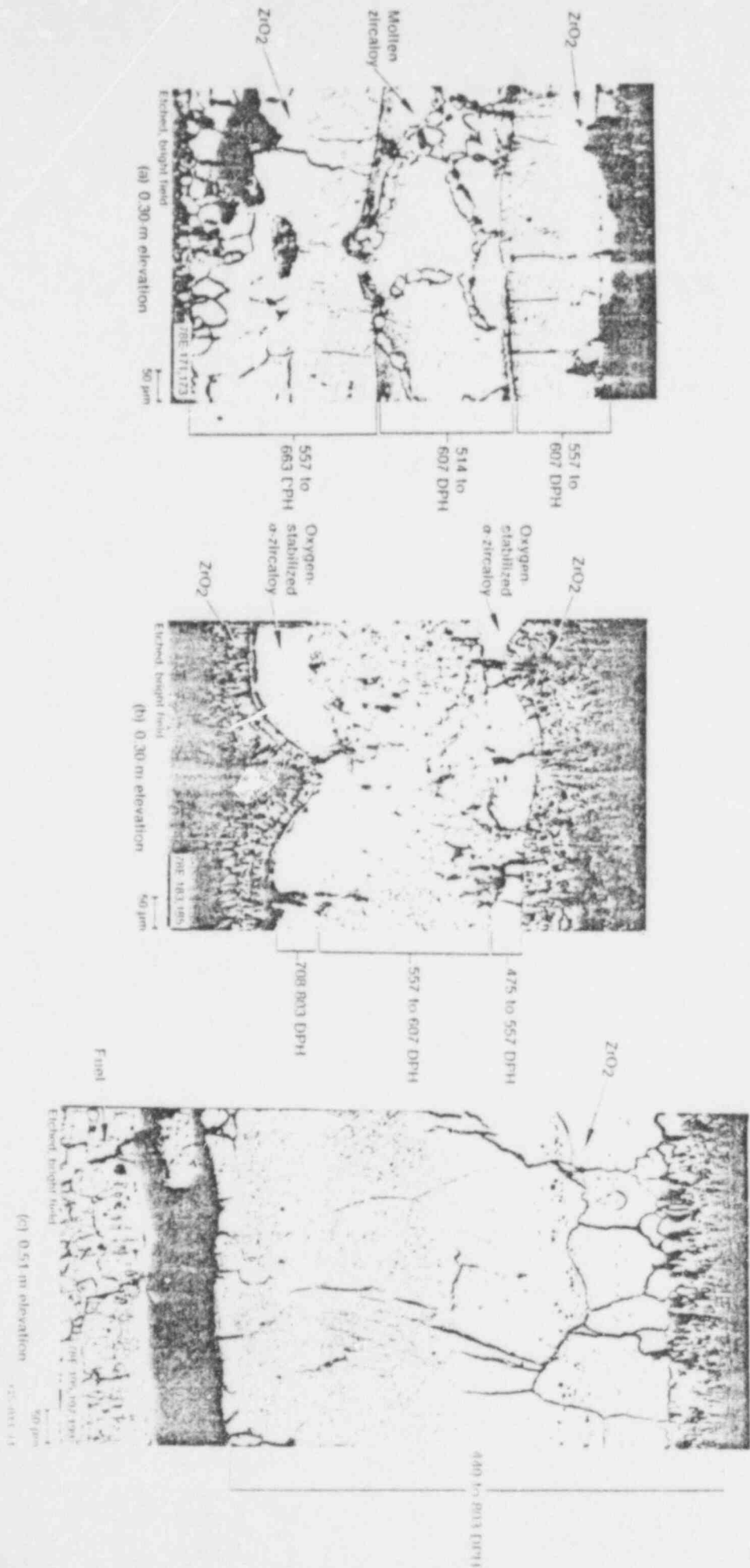
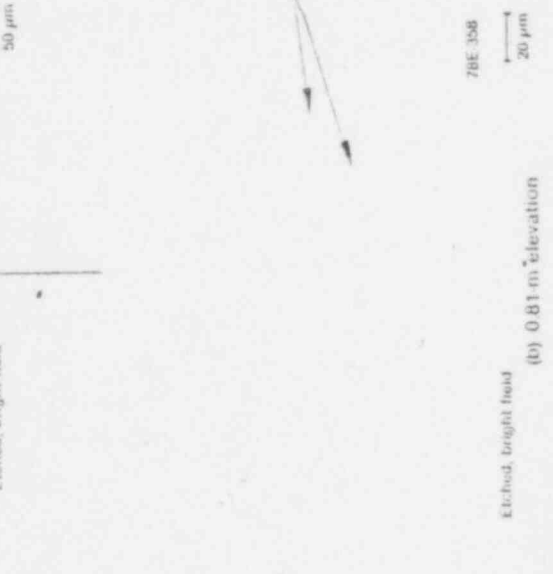
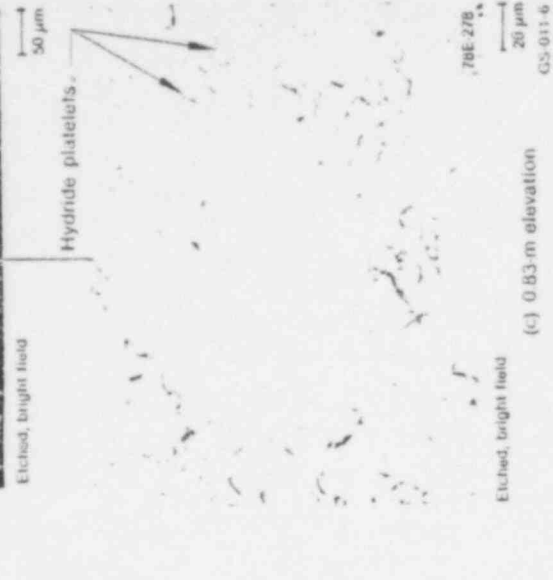


Fig. 22. Oxidation microstructures at 0.30 m and 0.51 m.



(c) 0.83-m elevation

(b) 0.81-m elevation

(a) 0.79-m elevation

Fig. 23 Hydriding in the stress-corrosion cracking near the top of the film boiling zone.

levels of 360 ppm were measured in the broken pieces of cladding from the high power region. The photomicrographs in Figure 23 indicate that the hydride platelets are thicker and more numerous in the cooler zircaloy structures (increasing content of equiaxed alpha). The hydride platelets are located along the edges of the prior beta grains in the alpha plus beta region at the 0.79-m elevation. The 0.81- and 0.83-m elevations are mostly recrystallized alpha-zircaloy, with a small amount of beta structure. The hydride platelets are found between the recrystallized alpha grains. By comparison with the embrittlement due to oxygen, the effect of hydrogen on fuel rod behavior during the extended film boiling operation in Test PCM-1 does not appear to be significant.

## VI. FUEL RESTRUCTURING

Film boiling transient conditions result in thermal restructuring of the  $UO_2$  fuel. The restructuring in Test PCM-1 fuel rod samples was characterized by equiaxed grain growth near the edge of the pellet; fuel melting as large as 85% of the pellet radius; porosity movement as a result of thermal gradients within the pellets; and fuel fracturing, shattering, and fragmenting as a result of the rapid heating and cooling of the test operation. The fuel rod failed during the test, exposing the fuel to a steam environment for an appreciable amount of time. Other features are also visible in the fuel that were probably due to chemical interaction of the  $UO_2$  with the steam environment. The following subsections detail the fuel porosity changes, melting characteristics, grain growth, grain boundary shattering phenomena, and probable chemical changes in the fuel.

### 1. POROSITY CHANGES

The Test PCM-1 fuel rod exhibited unusual porosity distributions in the fuel. Generally, a  $UO_2$  fuel pellet with centerline melting is characterized by a central void, although the central void may be filled due to fuel relocation as a result of melting. The region that cools rapidly upon final shutdown is indicated by a well-defined central region composed of a cellular substructure, sometimes containing spherical or tubular pores oriented in the radial direction. A pore-free, high-density band surrounds the central region. The outer boundary of the pore-free zone usually defines the maximum extent of melting, and is followed by a region of equiaxed grain growth, a region of grain boundary separation, and then, essentially unchanged fuel at the pellet periphery. The melt radius decreases with the restructuring of the fuel. Some migration of the initial porosity to the grain boundaries may occur<sup>18,19</sup>. This typical structure was not found in any of the five axial locations examined containing a molten fuel core. Examples of the fuel structure in the Test PCM-1 fuel are shown in Figure 24.

A central void was found at the 0.67- and 0.52-m elevations. A frothy appearing, extremely porous structure was observed at the center at the 0.30- and 0.59-m elevations. The porosity was probably due to shrinkage of the central molten zone upon rapid cooling at the end of the test. The pore-free region and equiaxed grain growth region at 0.30 m were significantly altered from the expected structures. These changes are thought to be a result of chemical changes in the fuel which are discussed in Subsection VI-5.

The pore-free region was not typical of what is generally observed at any of the elevations examined, possibly because of the increasing molten fuel radius due to the insulating effect of the oxidizing cladding. The randomly oriented, lenticular-shaped voids were also present at the 0.52-m elevation [Figure 24(a)]. At this elevation the pores were located in the region of limited equiaxed grain growth. The large, blocky grains which normally define the maximum extent of melting and are usually pore free contained, in this instance, porosity in the outer portion of the zone. This porosity may have been generated at the boundary between the maximum molten region and the solid region, and then migrated into the fuel during quench.

No central void was observed at 0.31 m [Figure 24(b)], although the beta-gamma autoradiography indicated a melt radius of approximately 56%. Some trails of pores were oriented radially as if voids had migrated to the center of the pellet; however, no true pore-free region existed. A band containing randomly oriented, lenticular-shaped voids was present at approximately two thirds of the pellet radius. Some voids may have been generated by cracks in the fuel; however, no obvious explanation is available for the generation of the lenticular pores and their random orientation at other locations.

The 0.59-m elevation exhibited a frothy center region, bounded by a pore-free region defining the extent of melting, and then a region of equiaxed grain growth. In the pore-free region a structure occurred that may have been either an unusual void formation or possibly a second phase. The structure appeared to be located primarily along cracks and grain boundaries. This structure is shown in Figure 24(c). Microprobe examination indicated no zirconium or tin in this region.



Fig. 14 Fuel porosity at several elevations.



Another unusual porosity distribution was found at the 0.67-m elevation [Figure 24(f)]. A beta-gamma autoradiograph of the cross section from this location indicated a melt radius of approximately 36% (Appendix C, Figure C-1). However, the grains were equiaxed to the center of the pellet with an even distribution of porosity across the radius. Some alignment of the pores along substructural boundaries within the large equiaxed grains may have occurred near the center of the pellet.

No compositional changes of the fuel were indicated by electron microprobe scans across the fuel at any elevation. If the unusual porosity distributions are due to compositional changes in the fuel, only slightly higher forms of the oxide must be involved. (Fuel chemical changes are discussed in Subsection VI-5.) Some of the porosity effects may be due to the cooling conditions of the fuel rod as the rod failed and was exposed to a steam environment internally. The porosity distributions observed did not appear to significantly affect fuel rod integrity during extended film boiling operation.

## 2. FUEL MELTING

Fuel centerline melting was extensive in the Test PCM-1 fuel rod. The largest melt radius found in the 15 elevations examined was 85% and was in a loose piece of fuel with cladding at the center of the rod. The molten fuel region extended from at least 0.304 (with a melt radius of 77%) to 0.670 m (melt radius 36%).

Cross sections of all of the exposed surfaces, both cut and broken, are shown in Figure 25. The elevations given for Figure 25(c) through (q) are the elevations at which the sections of the rod were located after the fuel rod shroud was split and opened and the fuel rod was examined. The space within the shroud was not sufficient for the rod sections to exchange places or turn end-for-end and, therefore, they are in the same order as they were during operation. The melt radii are plotted in Figure 26.

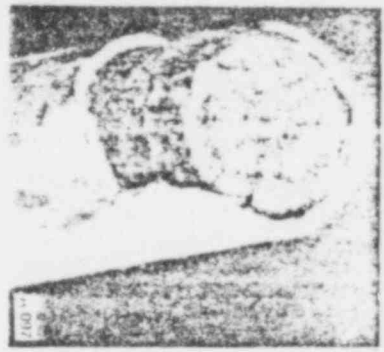
There were three rod sections without cladding that consisted of at least one intact fuel pellet. Generally, the melt radii were smaller at these locations than at locations where the cladding was still intact, indicating that the cladding had broken away from the fuel at some time before the rod was at the highest temperatures. With the cladding missing, heat transfer away from the pellets was improved; therefore, the centerline temperatures did not increase after that time. The fuel temperature increased at the locations with cladding because the continual oxidation of the zircaloy decreased the conductivity of the cladding and, therefore, insulated the fuel. Appendix F discusses the possible magnitude of the increase in fuel temperatures as a function of time at power.

Evidence exists of molten fuel being in contact with the cladding at 0.51 m. The molten fuel radius averaged 82% at this location, with the molten fuel in contact with the cladding at two positions. The fuel chemical changes as a result of this interaction are discussed in Subsection VI-5. There was no indication of molten fuel-cladding contact at any of the other elevations examined. The molten fuel did not seem to extrude through the cracks in the pellets, even at locations with a melt radius of as much as 85%.

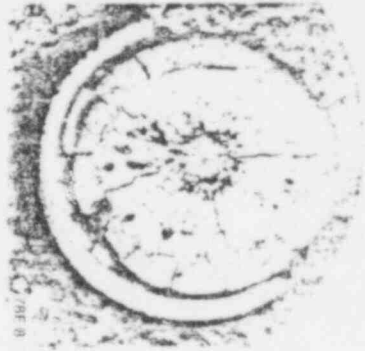
Despite the presence of large quantities of molten fuel, molten fuel-cladding interaction, and the access of steam to the rod interior, no evidence was found of preferential rod failures attributable to the molten fuel.

## 3. FUEL SHATTERING

Fuel shattering (grain boundary fracture) was observed at two elevations that were not exposed to steam. The shattering occurred at the outer 16% of the fuel pellet at the 0.67-m elevation and at the inner 64% at the 0.74-m elevation. There was central fuel melting at 0.67 m, but not at 0.74 m. The size of the equiaxed grains where the fracturing occurred varied from 3 to 46  $\mu\text{m}$  at 0.67 m and from 7 to 33  $\mu\text{m}$  at 0.74 m. Cross sections at these two elevations are shown in Figure 27. Fuel at two other elevations with similar grain sizes and fuel temperatures but which were exposed to steam were examined. No fuel shattering was observed at these locations.



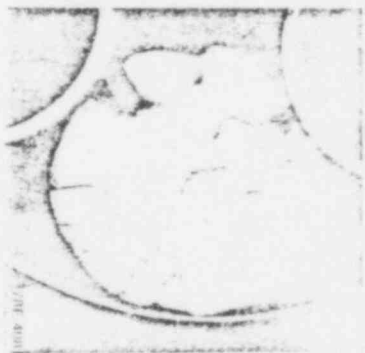
(a) 0.299 m elevation



(b) 0.297 m elevation



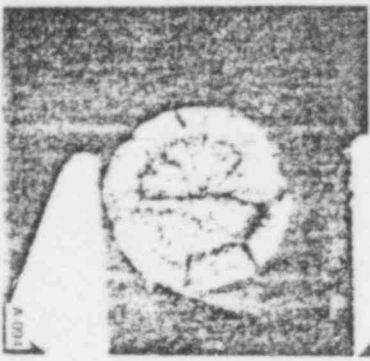
(c) 0.310 m elevation



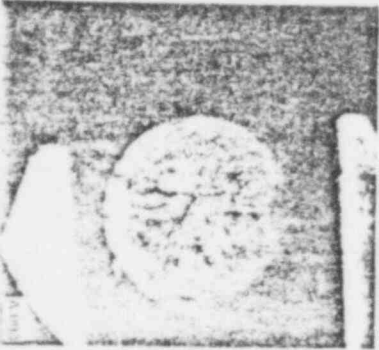
(d) 0.319 m elevation



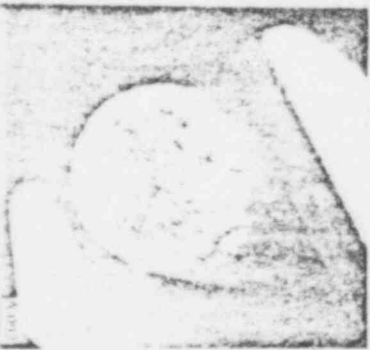
(e) 0.327 m elevation



(f) 0.433 m elevation



(g) 0.457 m elevation



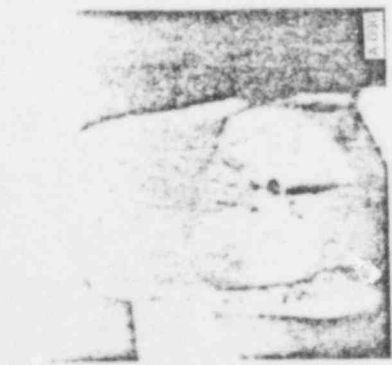
(h) 0.465 m elevation



(i) 0.490 m elevation

Fig. 28. A series of views of all examined fault surfaces.





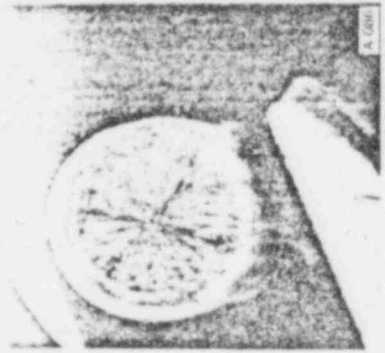
(j) 0.503 m elevation



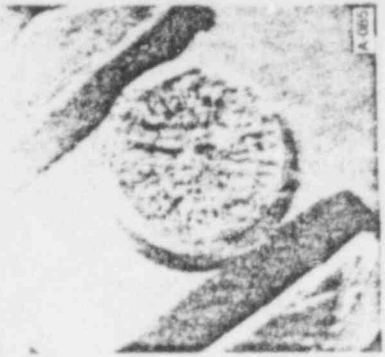
(k) 0.519 m elevation



(l) 0.519 m elevation



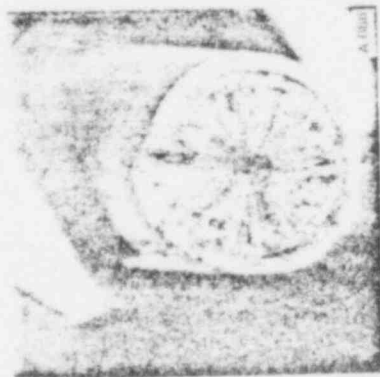
(m) 0.529 m elevation



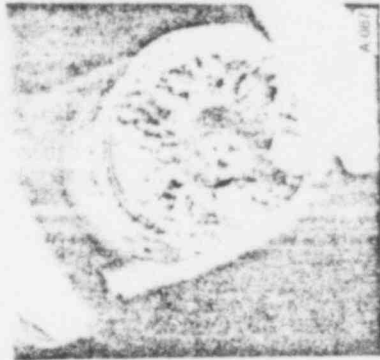
(n) 0.542 m elevation



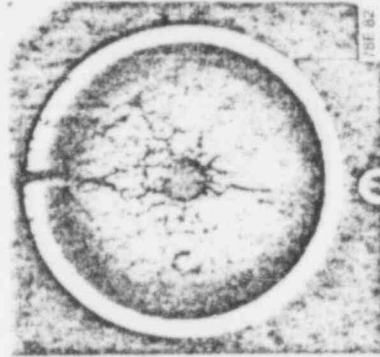
(o) 0.566 m elevation



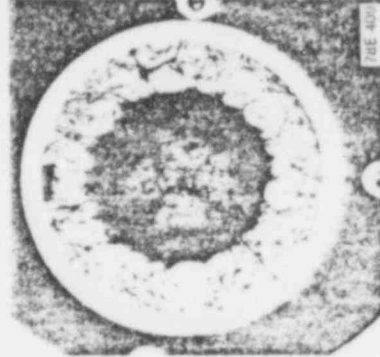
(p) 0.588 m elevation



(q) 0.630 m elevation



(r) 0.670 m elevation



(s) 0.743 m elevation

Fig. 25. Cross sections of all examined feet surfaces (continued).

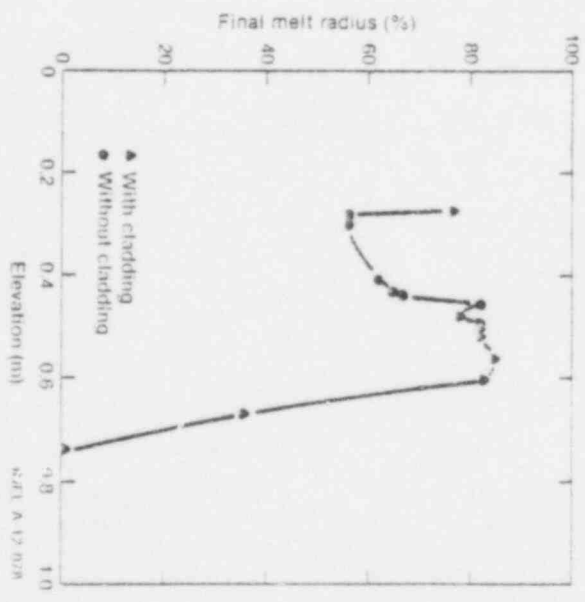
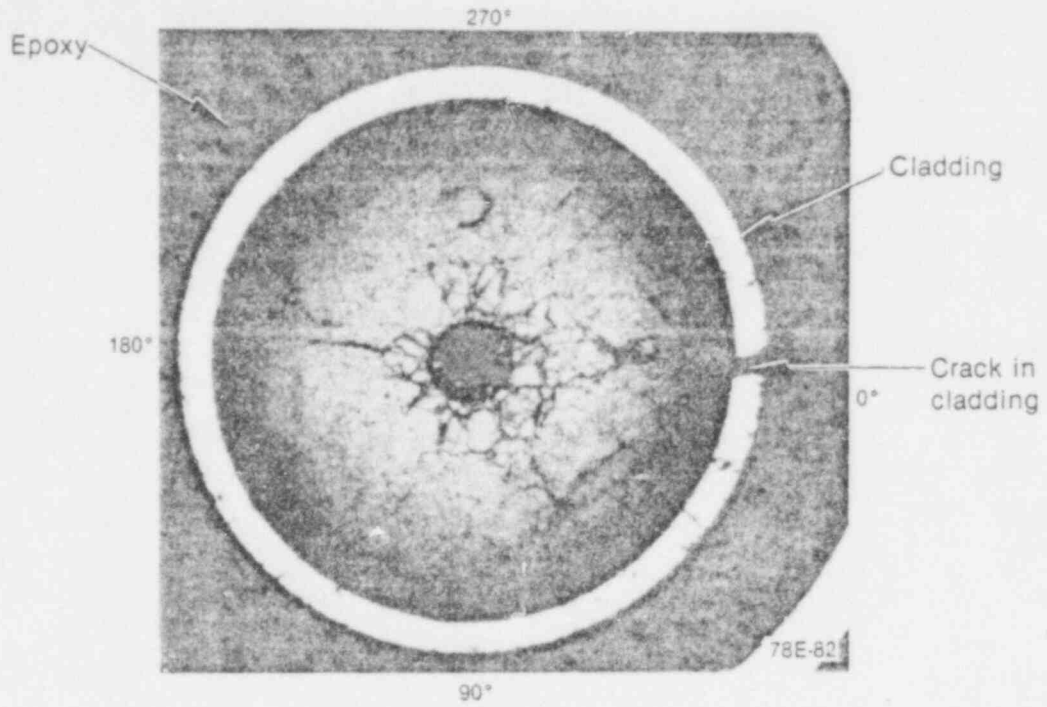
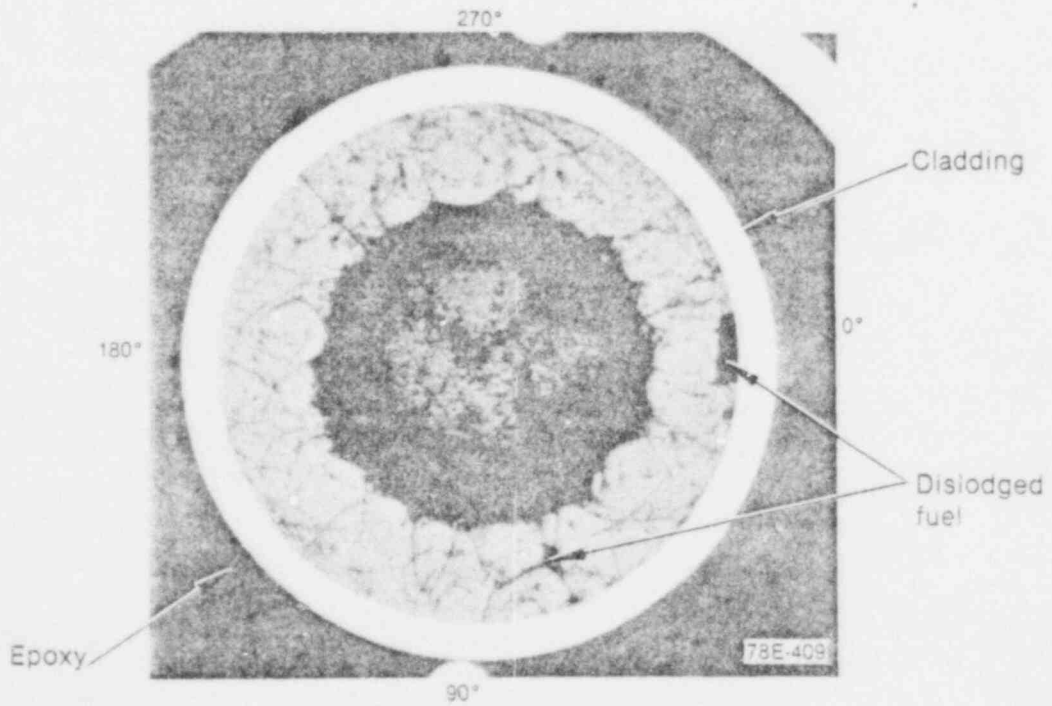


Fig. 26. Indentment data.



(a) 0.67-m elevation



(b) 0.74-m elevation GS-011-27

Fig. 27 Fuel shattering at 0.67 and 0.74 m.

Extensive fuel shattering did occur in the Test PCM-1 fuel rod since 24% of the fuel stack was reduced to particles smaller than 76  $\mu\text{m}$  and was washed out through the flow shroud particle screens. In accordance with an analysis<sup>20</sup> of fuel powdering (fragmentation) from previous PCM-type experiments, it is believed that the fragmentation occurred due to thermal stresses during the quench at test shutdown.

#### 4. EQUIAXED GRAIN GROWTH

The estimated temperature required for equiaxed grain enlargement in  $\text{UO}_2$  fuel is  $\sim 1900 \text{ K}$ <sup>18</sup>. This temperature is assumed to be characteristic of the boundary between unstructured and equiaxed grain zones. The temperature at which columnar grain growth occurs varies from 1970 to 2400 K, depending on the temperature gradient in the fuel. Fuel melting occurs at 3100 K.

Columnar grain growth did not occur at any of the elevations examined, even though there were regions of molten fuel present. Unstructured fuel at the pellet surface was found at the 0.67-m elevation and above. The grain size at the pellet surface, midradius, and center is given in Table VI for several elevations.

Fuel temperatures can be calculated from the fuel grain size, if the time at temperature is known, using the following equation<sup>9</sup>:

$$D^4 - D_o^4 = 1.717 \times 10^{10} t \exp\left(\frac{-3.87 \times 10^5}{RT}\right)$$

TABLE VI  
EQUIAXED GRAIN GROWTH

Elevation from the Bottom of the Fuel Stack (m)	Fuel Grain Size ( $\mu\text{m}$ )			Calculated Temperature (K)		
	Outer Diameter	Midradius	Center	Outer Diameter	Midradius	Center
0.299 -0.507	6	23	--	2000	2610	-
0.372 -0.580	16.5	50	--	2480	3160	--
0.670	3	46	--	1900	3090	--
0.743	3	7	33	1900	2060	2840
0.779 -0.798	3	5	11	1900	1930	2240
0.798 -0.817	3	3	5	1900	1900	1930
0.817 -0.836	3	3	3	1900	1900	1900

where

$D$  = final grain size,  $m$

$D_0$  = initial grain size,  $m$

$t$  = time,  $s$

$R$  = 8.314 (gas constant)

$T$  = temperature,  $K$ .

The temperatures calculated from the grain sizes are also given in Table VI. These temperatures may be somewhat high because of the accelerated restructuring as a result of increased oxygen content in the  $UO_2$ <sup>21</sup>.

## 5. CHEMICAL CHANGES

Chemical changes occurred in the  $UO_2$  fuel in Test PCM-1 as a result of the fuel exposure to steam for an extended period of time. The changes in chemistry of the fuel are of interest in order to evaluate the subsequent changes in the fuel properties, such as the melting temperature. The fuel chemistry changes were characterized by metallographic examination and microprobe analysis.

A precipitate was observed metallographically inside of the  $UO_2$  fuel grains at three of the elevations examined. This precipitate is believed to be  $U_4O_9$ . The U-O phase diagram (Figure 28) shows that  $U_4O_9$  does not exist above 1460 K at any O/U ratio. The fuel is in the form of  $UO_{2-x}$  above this temperature. Between O/U ratios of 2.0 and 2.25,  $U_4O_9$  exists below temperatures ranging from approximately 600 to 1460 K. The existence of  $U_4O_9$  is not clear for ratios above 2.25. The crystal structure of both  $UO_2$  and  $U_4O_9$  is cubic, with lattice parameters of 5.4704 and 5.4411 Å, respectively<sup>21,22</sup>.

The fuel structures at 0.52, 0.59, and 0.30 m are shown in Figures 29 and 30. These structures were compared with those reported by General Electric in Reference 22. The  $U_4O_9$  in Test PCM-1 had three slightly different appearances. At the edge of the fuel at 0.59 m [Figure 29(a)] and also at the edge at 0.52 m [Figure 29(b), (c), and (d)], the precipitates are large, angular structures within the  $UO_2$  grains. Closer to the center of the fuel, the precipitate is much finer, giving the  $UO_2$  a textured look at 200 X. Examination at higher magnification (500 and 1000 X) shows the angular  $U_4O_9$  precipitate in the  $UO_2$  grains.

The melt area in the fuel at 0.30 m had an unusual dendritic appearance, as shown in Figure 30. Calculations were made, using the oxidation rate equations given in Reference 21, at the pellet surface temperature determined from melt radius and local power. Sufficient time existed to diffuse oxygen to the center of the pellet in large enough quantities to convert a significant amount of the pellet from  $UO_2$  to  $U_4O_9$ , as shown by the calculations presented in Appendix G. The anomalous appearance of the molten fuel in Figure 30 may be due to the precipitation of  $U_4O_9$  upon solidification and cooling.

The presence of  $U_4O_9$  in the fuel at ambient temperatures indicates an O/U ratio in the fuel between 2.0 and 2.25. The melting point of the fuel is reduced and grain growth is expected to increase with the higher oxygen content. The net result of these effects is to increase the quantity of molten fuel; however, as previously stated in Subsection VI-2, no preferential rod failures attributable to molten fuel were observed.

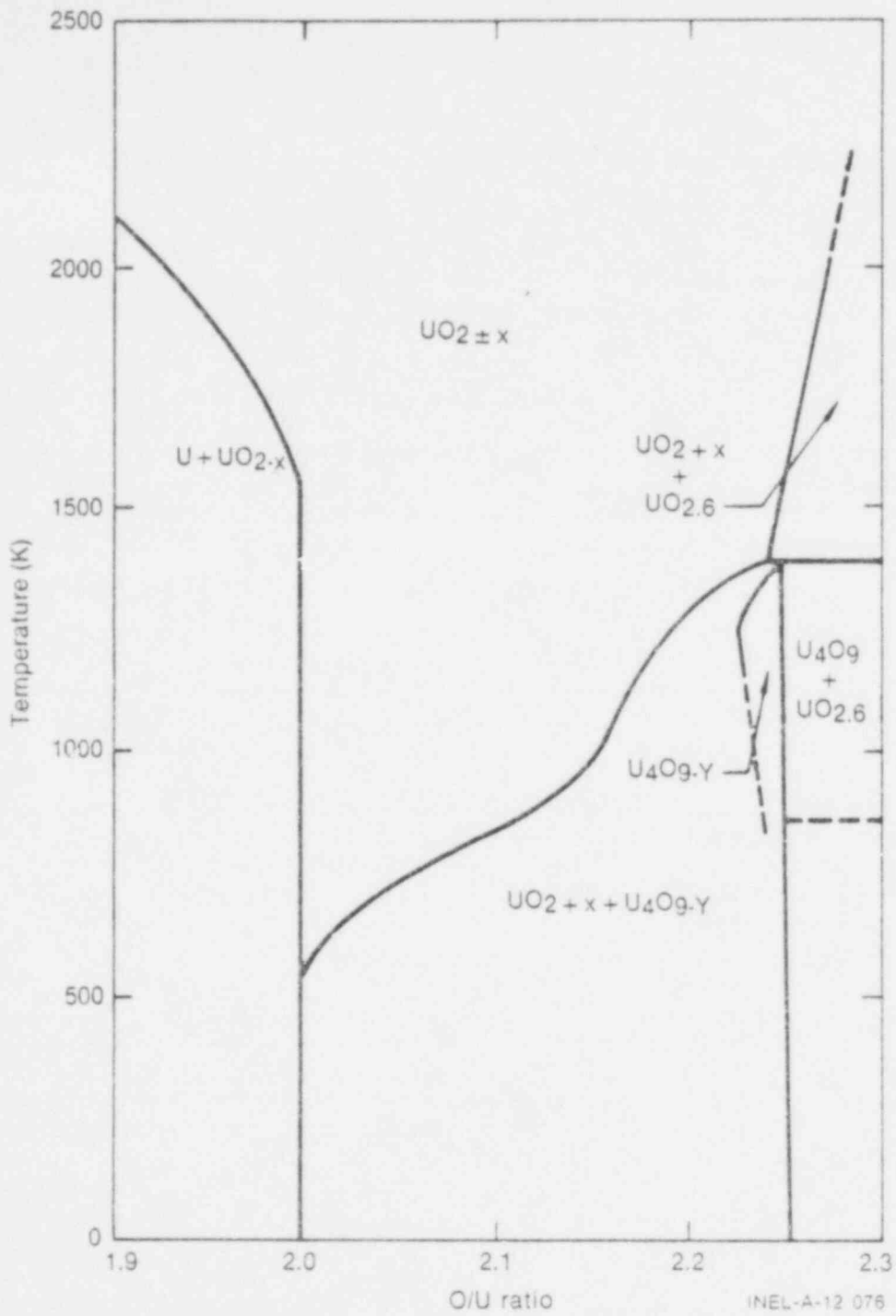


Fig. 28 Uranium-oxygen equilibrium phase diagram.



Fig. 29 Fuel structures at several elevations showing  $U_4O_9$  precipitates.

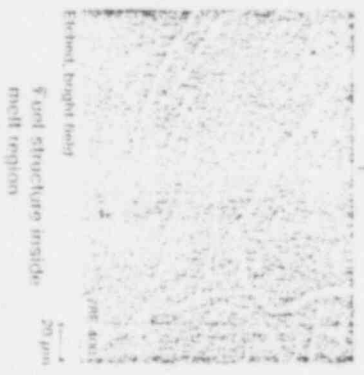
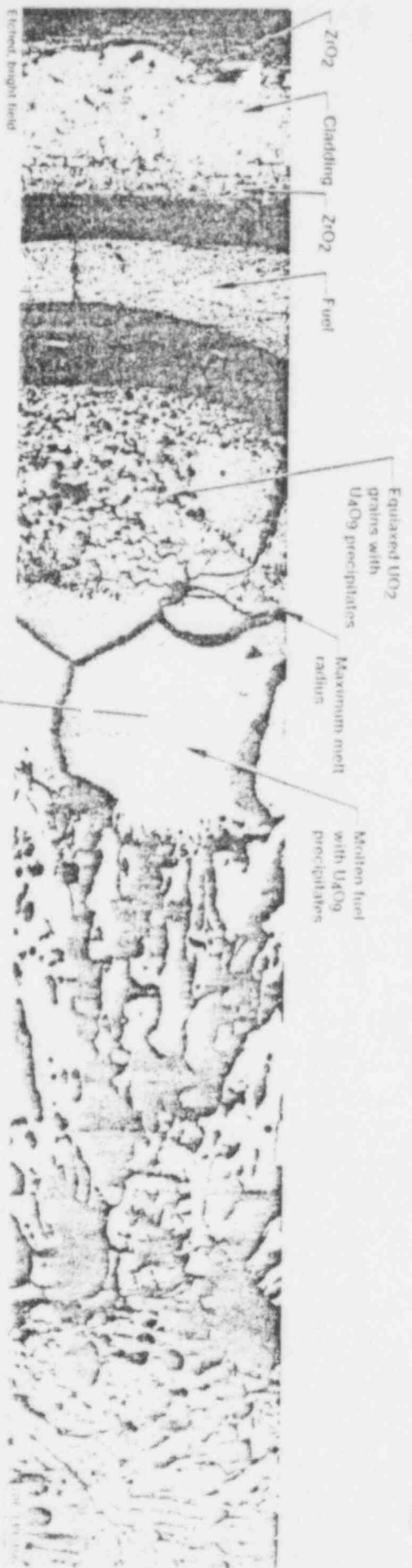


Fig. 10 Fuel structure at 0.30 m.

631 217



## VII. CONCLUSIONS

The objectives of Test PCM-I were to determine the time to failure of a single PWR-type fuel rod subjected to film boiling operation at higher power, investigate the mechanism of rod failure, examine any evidence of energetic molten fuel-coolant interaction and molten fuel related rod failures, and evaluate the behavior of a rod subjected to film boiling operation at high power following rod failure. The behavior of the fuel rod materials in the test, as it related to the test objectives, was analyzed on the basis of the post-irradiation examination. The fuel rod was operated in film boiling for 920 seconds; 280 seconds at 69 kW/m, and 640 seconds at 78 kW/m.

The fuel rod failed approximately 520 seconds into the film boiling transient by means of zircaloy cladding embrittlement due to oxidation. Extensive cladding fracturing occurred during film boiling. Fuel fragmentation resulting in the removal of 24% of the fuel stack from the flow shroud occurred, primarily during quenching at test shutdown. The flow shroud was not adversely affected by extended film boiling operation of the failed fuel rod. Cladding melting occurred over as much as 31% of the rod. The molten fuel region extended from at least 0.30 m (melt radius of 77%) to 0.67 m (melt radius 36%). Extensive fuel-cladding and cladding-coolant reactions occurred. Fuel-coolant interaction during film boiling operation resulted in oxidation of the  $UO_2$  fuel to  $U_4O_9$  in some locations; however, the compositional change, as well as the unusual porosity distribution, did not appear to significantly affect fuel rod integrity during extended film boiling operation. There was no apparent energetic molten fuel-coolant interaction.

Several general conclusions can be made concerning the operation of a fuel rod in film boiling for an extended time. Film boiling operation for extended times leads to extensive cladding oxidation which insulates the fuel, raising the fuel temperature and, therefore, increasing the extent of fuel melting. Extensive fuel melting (up to 85% of the pellet radius) does not seem to adversely affect the behavior of a failed fuel rod during extended film boiling operation. Cladding sections completely oxidized to  $ZrO_2$  and sections of molten cladding contained in a  $ZrO_2$  shell can maintain structural integrity. Limited structural integrity can also be maintained in unclad fuel sections.

## VIII. REFERENCES

1. United States Nuclear Regulatory Commission, Reactor Safety Research Program, *A Description of Current and Planned Reactor Safety Research Sponsored by the Nuclear Regulatory Commission's Division of Reactor Safety Research*, NUREG-75/058 (June 1975).
2. T. G. Odekirk, *Detailed Test Plan Report for PBF Test Series PCM-20: The Behavior of Unirradiated PWR Fuel Rods Under Power-Cooling-Mismatch Conditions*, ANCR-1095 (April 1974).
3. D. T. Sparks and C. J. Stanley, *Power-Cooling-Mismatch Test Series Test PCM-1, Fuel Rod Behavior Report*, to be published.
4. R. B. Roemer, "The Effect of Power Transients on the Peak Heat Flux," *International Journal of Heat and Mass Transfer*, 12 (1969) pp 953-964.
5. D. E. Thornton and D. H. Schwieder, *Experiment Data Report for Test PCM-1*, NUREG/CR-0292, TREE-1233 (September 1978).
6. P. D. Randolph et al, "Measured Fission Product Release During Power-Cooling-Mismatch Induced Failure," *Transactions of the American Nuclear Society*, 29 (Winter 1978).
7. J. B. Cathcart et al, *Zirconium Metal-Water Oxidation Kinetics IV Reaction Rate Studies*, ORNL/NUREG-17 (August 1977).
8. M. S. El-Genk, *An Assessment of Fuel Melting, Radial Extrusion, and Cladding Thermal Failure During a Power-Cooling-Mismatch Event in Light Water Reactors*, NUREG/CR-0500, TREE-1270 (April 1979).
9. P. E. MacDonald et al, *MATPRO - A Handbook of Materials Properties for Use in the Analysis of Light Water Reactor Fuel Behavior*, ANCR-1263 (February 1976).
10. S. L. Seiffert and R. P. Hobbins, *Oxidation and Embrittlement of Zircaloy-4 Cladding from High Temperature Film Boiling Operation*, NUREG/CR-0517, TREE-1327 (April 1979).
11. P. Hofmann, C. Politis, "Chemical Interaction Between  $UO_2$  and Zry-4 in the Temperature Range Between 900 and 1500°C," *4th International Conference on Zirconium in the Nuclear Industry, Stratford-On-Avon, England, June 26-29th, 1978*.
12. P. Hofmann, *Konstitution und Reaktionsverhalten von LWR-Komponenten beim Coreschmelzen*, KFF 2242 (February 1976).
13. C. J. Scatena, *Fuel-Cladding Embrittlement During a Loss-of-Coolant Accident*, NEDO-10674 (October 1972).
14. P. D. Parsons, "Zircaloy Cladding Embrittlement in a Loss-of-Coolant Accident," *Sixth Water Reactor Safety Research Information Meeting, Gaithersburg, Maryland, November 6-9, 1978*.
15. D. O. Hobson and P. L. Rittenhouse, *Embrittlement of Zircaloy-Clad Fuel Rods by Steam During LOCA Transients*, ORNL 4758 (January 1972).
16. R. R. Hobbins et al, "Zircaloy Cladding Behavior During Irradiation Tests Under Power-Cooling-Mismatch Conditions," *American Society for Testing and Materials, ASTM STP 633 (1977) pp 182-208*.

17. A. Sawatzky, "Hydrogen in Zircaloy-2: Its Distribution and Heat of Transport," *Journal of Nuclear Materials*, 2 (1960) pp 321-328.
18. D. R. Olander, *Fundamental Aspects of Nuclear Reactor Fuel Elements*, TID-26711-PI (1976).
19. M. D. Freshley, "Operation with Fuel Melting," *Nuclear Engineering and Design*, 21 (1972) pp 254-263.
20. A. W. Cronenberg and T. R. Yackle, *An Assessment of Intergranular Fracture Within Unrestructured UO<sub>2</sub> Fuel Due to Film Boiling Operation*, NUREG/CR-0595, TREE-1300 (March 1979).
21. J. T. Bittel et al, "Steam Oxidation Kinetics and Oxygen Diffusion in UO<sub>2</sub> at High Temperatures," *Journal of the American Ceramic Society*, 52 (8) (1969).
22. *Sixth Annual Report — High Temperature Materials Program*, GEMP-475 A (March 31, 1967) pp 251-256.

DISTRIBUTION RECORD FOR NUREG/CR-0757  
(TREE-1333)

Internal Distribution

- 1 - R. J. Beers, ID
- 2 - P. E. Litteneker, ID
- 3-5 - INEL Technical Library
- 6-7 - Author
- 8-50 - Special Internal

External Distribution

- 51-56 - Special External
- 57-58 - Saul Levine, Director  
Office of Nuclear Regulatory Research, NRC  
Washington, D.C. 20555
- 59-355 - Distribution under R3, Water Reactor Safety Research -  
Fuel Behavior

KUREG/CR-0/5/  
TREE 133  
UNCLASSIFIED

APPENDIX A thru G  
DURING TEST PC M-1

FUEL ROD MATERIAL BEHAVIOUR  
B.A. COOK 6/79 EG&G

